JOTCS
Journal of the Turkish Chemical Society
Section: B
Chemical Engineering
TURKISH CHEMICAL SOCIETY

EFFECTS OF FUEL PROPERTIES AND SPRAYING FLUID ON GASOLINE ENGINES

Cemil Koyunoğlu[1], Fikret Yüksel[1,*]
[1]Yalova University, Faculty of Engineering, Department of Energy Systems Engineering

Abstract: In this study, the ignition delay measurement was determined numerically by using some practical equations. Outboard ignition engines take the fuel-air mixture into the cylinder and compress it. High compression ratio is an important parameter that increases engine efficiency. The compression ratio is kept away from the knock limit, which is also defined by self-ignition of the mixture. The ignition system should be able to initiate combustion without igniting the mixture at the appropriate moment and causing undesired mechanical and thermal stresses. The temperature at the tip of the spark plug at the time of ignition is proportional to the blur of the gauge voltage and usually ranges from 500-800 °C. A well-working flue gas should have a porcelain temperature of less than 500 °C and no more than 850 °C. The temperature at the end of the isolator is crucial for the development of ignition and combustion. Higher tip temperatures, premature ignition, and low temperatures cause spark plug contamination and kicking. Accumulation of unburned or slightly burnt hydrocarbons in the interior of the buoy is indicated as the responsibility of the contamination and therefore the singlet. Hydrocarbon deposits reduce electrical insulation too much over time, preventing the syringe from forming between spark plug nails. In our work, evaluations were made on hydrocarbon deposits in terms of insulator temperature and system self-cleaning temperature and so on.

Keywords: Fuel properties, Gasoline engines, Spray injection, Knock, Octane number.

Submitted: April 12, 2018. **Accepted:** September 14, 2018.

Cite this: Koyunoğlu C, Yüksel F. EFFECTS OF FUEL PROPERTIES AND SPRAYING FLUID ON GASOLINE ENGINES. JOTCSB. 2018;2(1):1–12.

Corresponding author: Fikret Yüksel, fikretyuksel@yahoo.com.

INTRODUCTION

Knowledge of the time to ignition upon sudden heating of a fuel-air mixture has immediate practical significance relative to the performance of some air-breathing engines and other high-intensity combustion systems (1). Measurements of ignition delays (or induction periods) in the laboratory have recently been carried out mainly with shock tubes, which provide virtually instantaneous heating of a gaseous fuel-oxidant mixture, Shock tube data further provide an important experimental reference for kinetic modeling, very analogous to flame profile data but possessing the great advantage from the chemical standpoint that transport of species and energy is negligible because of the very short times (microseconds to milliseconds) involved in the shock tube observations (2). Thus the equations to be solved are considerably simplified (3).

There are some difficulties in this approach. First, there is the experimental problem of defining the moment of ignition (*e.g.,* of a hydrocarbon-oxygen-diluent mixture) in shock waves, the features followed maybe the pressure, the concentration of one or more radical species (*e.g.,* OH) as measured by light adsorption, the emission from excited OH; CH, or C_2, or a combination of these (2). The end of the induction period is associated with rapid but not discontinuous increases in these features; hence the definition of the moment of ignition is necessarily somewhat arbitrary. Investigators usually choose to define it in a way that will yield consistent results and permit comparisons with theory. This one might, for example, take it as the moment when the OH concentration reaches some particular value (2).

Assuming that the delay has been well defined, one measures it in shocks having a wide range of compositions, temperatures, and pressures. A correlation is then sought among the variables that will produce a straight line on an Arrhenius-type plot. Thus Serry and Bowman (1970) found the most satisfactory correlation of their data on methane ignition to be given by

$$t[O_2]^{1.6}*[CH_4]^{-0,4}=A\exp(E/RT) \quad (1)$$

where t is the ignition delay time and A and E are constants. This plot alone may well serve as a useful empirical correlation that will permit predictions of ignition delays. Its value becomes greater if one proceeds to kinetic modeling of the ignition process. The objective is, of course, to reproduce the empirical correlation (4). The modeling consists of a computer program by which the coupled differential equations of chemical kinetics and the gas dynamic and state equations are numerically integrated, yielding the time dependence of all pertinent variables: concentrations, pressure, and so on. The analytical results for the induction times can then be compared to the experimental values for various starting conditions (1).

GASOLINE ENGINE

It has been attempted to increase gasoline production by breaking down heavy parts on the need to increase the petrol requirement and not to meet the petrol requirement, which is obtained only by the distillation of crude oil (5). Despite the fact that this cracking process precedes only to increase gasoline production, it is understood that the gasoline obtained in this way has a higher octane number. Thus, higher octane gasoline was found to have a higher octane number (6). Thus, high-compression, highly efficient engines are made with the benefits of high octane gasoline (see Figure 1.) (7).

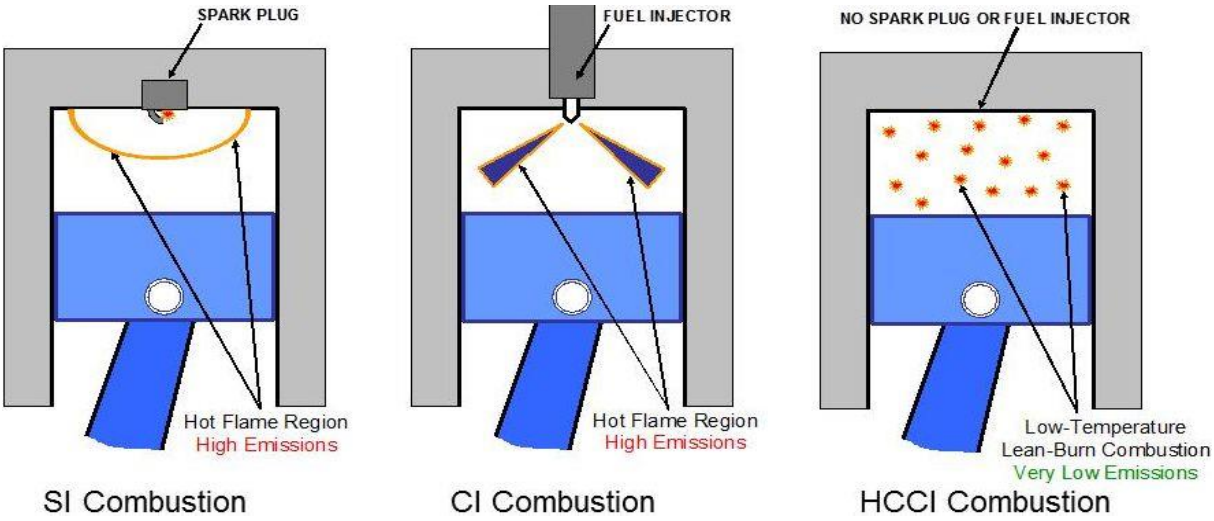

Figure 1. Homogeneous Charge Compression Ignition (HCCI) engines (2015).

During the operation of a four-stroke gasoline engine;
a) Suction
b) Compression
c) Enlargement
d) Exhaust
movements must be examined. Each of these movements is represented by a stroke, and these four strokes are completed in two cycles of the crank to provide useful work (8). The expansion stroke is also called work stroke.
Suction and Compression were examined in detail in the relevant sections separately, but the enlargement and exhaust events were presented together.

Suction stroke
The piston moves from the upper dead point (U.D.P.) to the lower dead point (L.D.P.) on the intake stroke. During this movement of the piston, the volume that is generated in the cylinder comes to grow with a vacuum. Due to this vacuum, the outside air enters the cylinder through the intake valve which is opened by passing through the air filter and the carburetor. The flow rate of this air entering the cylinder depends on the engine speed, the piston speed, and the channel cross-sections in the passages. When the speed change of the air passes through the carburetor, it flows into the bubbler, and when it passes through the carburetor, it moves in the direction of the fluid, and as it passes through the venturi throat in the carburetor, the velocity increases and hence the pressure decreases. This pressure drop is below the atmosphere at the point where the cross section is narrow. Since the pressure in the capillary gas cylinder present in the carburetor is always an atmosphere, the gasoline in the carburetor sprays into the air going into the cylinder because of this pressure difference. Under pressure, a low-pressure medium is sprayed from a capillary nozzle and the gasoline is evaporated by immediately separating it into small particles. The mixture of air and vaporized petrol brings the mixture to the water line and the mixture is sucked into the piston during suction stroking; this stroke ends with the piston sinking to the bottom dead point. In the meantime, the crank has made half a cycle (9).

Compression stroke
Following the completion of the suction stroke, the pistons that have come up to this time are now in the L.D.P. move from U.D.P. and it starts to compress the mixture which is filled in the cylinder slowly. By compressing the mixture into the increasingly constricted volume, the pressure and temperature rise and the piston U.D.P. the mixture with the spark plug is ignited.

Enlargement and exhaust
Before arrival of the piston U.D.P., the reasons for the start of the ignition are as follows:
a) Burning event, piston U.D.P. and the pressure drop due to the expansion action of the piston is the result of the inability to reach the expected burning. For this reason, the piston U.D.P. is necessary to take into account the combustion of the fuel.

b) The high pressures resulting from the expansion combustion increase the piston speed to 25-30 m/s by adding a new pressure to the downwardly moving piston and gain

power to the piston. This piston is the third stroke and the work stroke and crank complete the first half cycle of the second turn.

c) After completing the exhaust expansion stroke, that is, at the end of the movement in which the work is obtained, have arrived. This burning is finished and the exhaust valves are opened. U.D.P. This movement of the piston moving upward from the exhaust gas is discharged to the outside of the exhaust valve. Since there is no counter pressure, in this case, the operation is very easy. The piston moves in the direction of U.D.P. the fourth stroke is completed and the crank completes the second round at this time to obtain the work (10).

KNOCK

When an explosive device such as a gas-air mixture is ignited with a spark, the part near this spark is first ignited. This burning eventually increases the pressure and temperature of the other parts. The flame spreads in succession to other parts at a speed of 25 m/s and when one part burns, the pressure and temperature of the rest increase more. As this burning continues, the unburned gases become easier to ignite as a result of the temperature rise caused by the burned part. Because of this pressure and temperature rise, mixtures far away from the flame front are self-igniting and combustion becomes abnormal. Thus, the pulsating waves go to the cylinder face, the pistons and the cylinder head to hit the undesired phenomenon called "knock". As a consequence, we see that the reason for the knock is due to the pressure and temperature exceeding a critical limit. The sudden increase in pulse waves, high pressures and rapid increase in pressure after such a boundary are explained as follows: At the beginning of combustion, other peroxides and aldehydes form carbon monoxide (CO) and carbon dioxide (CO_2). These compounds, which are very unstable, burst at a critical pressure and temperature, bringing them to the pulse, the knocker. These peroxides depend on the type of chemical that burns. This means that aromatic hydrocarbons that are slow-burning and heavy, bring less knocking than light but fast burning paraffins. The knock is further dependent on the distance the flame spreads to the mixing parts. The bigger this distance, the quicker it will be because the knock will reach the critical value without the last flame coming out. Compression chambers in the form of hemispheres delay the detuning (11).

The knock is very harmful for the following reasons:
1- The maximum pressure is sudden and very high, which causes a severe impact on the engine. This dynamic effect vibrates the elastic parts of the engine and causes the piston to collapse after a period of time.

2- Due to the high temperature, the pistons are defeated after a while, especially at the places where they meet the knocking, and they break long after long. Since the pulsation raises the piston face and, if necessary, the gas boundary layer over the cylinder rings, the thermal conductivity coefficient increases, the piston becomes very hot, and the cylinders cause the cooling water or air to become very hot.

3- Because the temperature is too high, some of the carbon from the depression will burn out into black smoke.

4- Motor power is reduced.

5- Since the temperature in the cylinder is very high, the mixture ignites spontaneously without reaching the end of compression and without sparking, and the engine works very irregularly, causing great shaking. This is called spontaneous ignition (12).
It depends on the type of hits you burn. Some hydrocarbons, like n-heptane, are very prone to knock. These are called knockers. Some of them are resistant to knocking, which is also called non-knocking. Iso-octane is the one of this kind. At this point, these two classes of hydrocarbons can be mixed with each other in different amounts to obtain different fuels.

There are some chemical compounds, which when added to benzene, reduce the knock, which is called knocking. Hydrocarbons comply with the following sequence in terms of knock resistance.
1. Aromatics,
2. Isoparaffins: Unlike regular paraffins, they show a branched structure, so they are very difficult to break down. Knock resistance is high.
3. Cycloparaffins (Naphthenes),
4. Olefins,
5. Normal paraffins,
The scale correctly indicating the knock resistance of the burners is the "octane number" (12).

OCTANE NUMBER

When the engine is running, the piston is fully raised. The volume between the cylinder and

the cylinder head is called the "compression ratio" of this engine to the rate of volume remaining in the cylinder when the piston is fully down. For petrol engines, this ratio is at least 1/6, at most 1/12 today (13).

The air-gasoline mixture that is sucked into the cylinder must rise to a temperature that it will not self-immobilize during this compression, and the firing time of the spark must be well calculated. If the ignition time of the buzzard is normally delayed or occurs beforehand, then the burners will make a hammer stroke on the piston. It is called knock. It is closely related to the octane number of the gasoline (14).

In engines with high compression ratios, the use of low octane gasoline results in knock and knocking problems (15).

In vehicles with compression ratios, the use of high-octane gasoline, which is engine-intensive octane gasoline, reduces knock-out and removes knock-outs. Higher octane gasoline is more costly, and when used in engines with compression ratios, increases efficiency and power, reducing fuel consumption. This saves fuel costs. For example, if you use 85 octane gasoline and 80 octane gasoline with a compression ratio that is reasonable to use, there will be a decrease in efficiency and strength. If 85 octane gasoline is used, the fuel consumption is reduced by 3% with the increase in efficiency and power (10).

As a result, using a gasoline engine instead of low octane gasoline in a certain motive, it reduces the knocking sickness and provides a reduction in fuel consumption to provide equal power (14).

The above benefits are not obtained if higher octane gasoline is used that is necessary in low compression ratios. When engines with low compression ratios use a gasoline on the required motor, there is no knock due to the fuel. When high-octane fuel is used, there is no increase in efficiency and power (10).

Although a power boost can be provided by slightly increasing the ignition advance of the engine, it can be manufactured for a certain power, but the motor produced for a given power is excessively forced and the motor life is shortened due to excessive force. The use of high-octane gasoline in such an environment is not economically viable either (10).

As it increases from sea level, the need for octane decreases for every 300 m. A decrease in the number of octanes for height is required 3500 m. This value is 300 m. for 7-7.5 units (14).

Because some engines with suitable structure use higher octane fuel, more power can be obtained. However, as high octane fuel in normal transportation is used, we can not get extra power and speed. Under some operating conditions, when increasing the number of octane to 68 denier, it is seen that there is a 15% increase in the speed of the car, but there is no rapid development or even a decrease in some other types of cars (10).

In our country, there are approximately 600,000 gasoline-powered vehicles, 75% of which have compression ratios of 1/7.3 and 80 octane gasoline. In recent years, high-octane (87-90) petrols have been supplied to the market in order to meet this demand in other countries due to the increase of high-compression-ratio vehicles. There is even a 100-octane gasoline in America (14).

Determine the number of octanes

The ability of the gas to burn uniformly without knocking on the motor is specified by the number of octane. There is a jam in the cylinders during the movement of the engine piston. If the space left in the cylinder just above and above the piston during the upward and downward movement of the piston is 1/6 of the space at the bottom of the piston, the compression ratio of this engine is called six times. During this compression, the temperature of the mixture increases. This ratio is adjusted so that the temperature of the mixture does not reach the point where it can burn itself. (The gas-air mixture reaching a certain pressure and temperature can start to self-ignite even without sparking) (15).

Increasing the compression ratio increases its efficiency and power. If the compression ratio is lowered, the mixture burns more appropriately. In other words, it is more slowly and relatively tactile, and it is more appropriately lit. So it is a slower and relatively tactical combustion. In turn, the resulting power is reduced (10).

As can be understood from the above explanation, the gas vapors in the combustion chamber increase in relative power and efficiency, which can be compressed before igniting. Since this compression rate is limited, it can not be compressed anymore (5).

In today's gasoline engines industry, great emphasis is placed on high-compression engines because stronger and faster cars are in great demand (10). That is, as the compression ratio is raised, the probability of a uniform combustion is reduced, a sudden combustion occurs. It explodes briefly. At the beginning of combustion, aldehydes and peroxides are formed beside CO and CO_2. These chemical substances, which are very unstable, can not burn under pressure and temperature, but they explode. This event can occur at several places in the combustion zone. This is called "Knock". We can compare it to a hammer crush, which is down to the piston. Only a small fraction of the energy generated at such an uneven side is converted into useful energy. Much of this is tired of parts of the machine and parts. The only thing to do is to control the burning of the gas. If you have to produce a fuel that will burn evenly under high compression (even if it is stuck), it shows resistance to sudden burns, explosions, impacts and knocking. This type of combustion is achieved only with high octane gasoline. As we have said above, the characteristic of a gasoline to burn uniformly without knocking on the motor is indicated by the number of octane (14).

In order to increase the resistance of the gasoline to knocking, it is provided either by making a change in the inside of the molecule to convert it into a more or less aromatic or isoparaffinic form, or by the addition of carburizing units with very slow oxidation of benzene and by the addition of benzene lead tetraethyl (8).

There is a misunderstanding among the people about the issue of octane; high-octane gasoline is thought to be a gasoline type that burns more easily than a low-octane gasoline and can easily burn. Such an idea is wrong, and the opposite is more or less the case. The number of octane in the gasoline is determined by the single-cylinder, special octane engines located in the fuel oil laboratory. The compression ratio of this motor can be adjusted to the desired state (9).

There are different methods to be applied for the test. It should be indicated that the method has been applied firstly. The fuel to be assigned to the engine is filled into the engine's tank and the engine is started. Whichever method is applied, the values indicated by the method are provided (engine revolution and gasoline inlet temperature of the engine). The compression ratio is changed to bring the motor to the knocking stage. The amount of knock is determined by the "knock meter". The engine is stopped. The fuel which is being tried to be assigned to the boiler is discharged. Instead, reference fuel prepared in different proportions (iso-octane + n-heptane mixture) is filled. The engine is started. Since the compression ratio remains unchanged the cycle and temperature (gasoline engine inlet temperature) are set. This reference fuel mixture ratio is iso-octane + n-heptane. Various experiments are carried out by varying the n-heptane quantities so that you get the same amount of knock under the same conditions. The reference octane number in the reference fuel mixture, which gives equal knock to the gasoline knock to be assigned to the octane, is 100 (octane number) and the normal heptane is zero (0) (14).

For example, if an equal knock of a gasoline knocker gives a mixture of 95% iso-octane and 5% n-heptane, the octane of the fuel is 95 [9].

PRE-IGNITION

The hot spark plugs, hot carbon deposits, or the cylinder head does not cool properly form a number of hot spots in the combustion cell. These points act like a spark plug. In fact, at the end of the compression time, it is only through the spark plug that it is inevitable that it starts at these hot spots. So instead of burning is an explosion. The knocking from the square is also called the early firing knock. There is nothing to do with the knocking that comes from fuel quality (14).
The knock from the fuel quality decreases as the engine revolves. The knocking from the early ignition increases the engine revolutions by an order of magnitude [8].

To increase the octane number of the gasoline:
a) Lead Tetra Ethyl (TEL):
The most appropriate amount is 1. gallon gasoline 3 mL. There are some drawbacks to using octane in order to increase the number (10).
E.g:
a) Lead oxide formation at the engine combustion site.
b) Spark plug clogging, short circuit, and consequently loss of power
c) If there is no special design, the exhaust valve burns,
d) It is too toxic.
"Ethylene bromide" is added to prevent the harmful effects of lead, which becomes

gaseous lead bromide, easily removed from the suploat (10).

b) Benzene

The octane number can be increased by mixing 10% of unleaded benzene with pure benzene. However, as mentioned before, benzene is harmful because it is an aromatic substance and will destroy other qualities of gasoline (14).

c) Alcohol

In countries with high alcohol consumption, alcohol is mixed to increase the number of octane. For example, if the 67 octane gasoline is mixed with 20% alcohol, the octane number is 78 to 80. This should be in the purity of alcohol (100% - 96%). The only problem is that it is expensive and the water present in the alcohol decomposes and rusts on the surface of the metal (15).

IGNITION DELAY

There are two types of combustion in internal combustion engines or appliances. The first is that the reactive mixture is ignited from the outside (pilot flame, spark plug etc.) and the reaction of the born flame ceiling continues. The other is to prepare the reactive system thermally and actively for the reaction and to ensure that the ignition is spontaneous (see Figure 2.) (13).

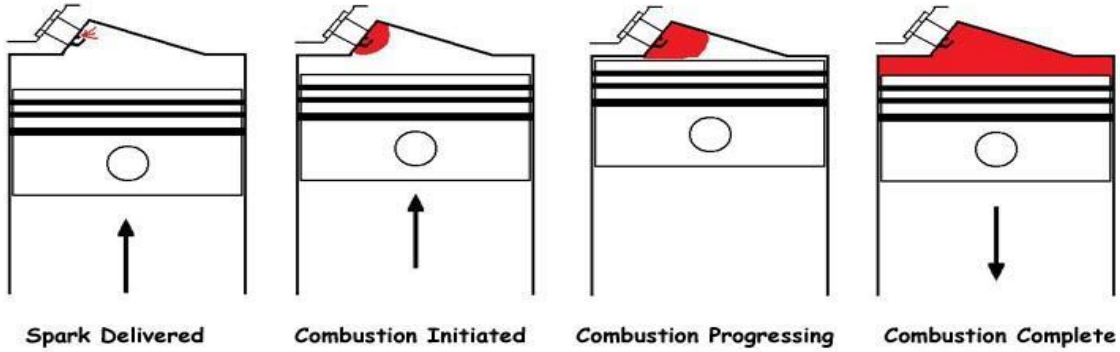

Figure 2. Typical ignition process (2015).

Because the fuel-oxidant system does not self-ignite in gasoline engines, gas turbines, and some rockets and ramjet engines, high kinetic energy electrons (spark) are delivered to the molecules in the system by a spark plug. Thus, the disintegrating molecules give the active ingredients (H, O, OH, CH_3, CHO, etc.). These active ingredients give exothermic reactions to the stable molecules and reveal a luminous region at high temperature called the "flame front" (In particular, it depends on the genus of the light). Since the flame ceiling is at high temperature, 2000-5000 K, molecules accelerate the entry into the reaction and maintain the event (see Figure 3 for the combustion problems) (13).

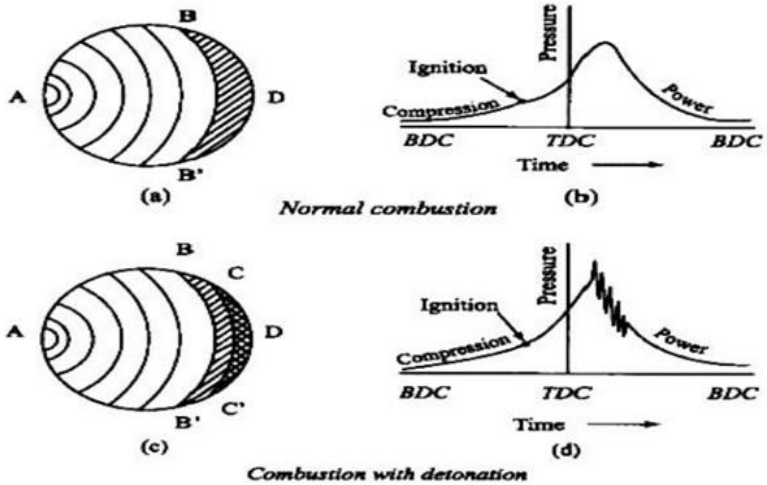

Figure 3. Normal (a,b), abnormal (c) combustion and problems (d) (Poonia 2014).

In diesel engines or some rockets, the system is designed to show self-ignition. That is, when the oxidant and the reactant come together, there can be reactions between the molecules in the temperature and concentration conditions. However, for a noticeable increase in temperature or pressure, a certain preparation time is passed which is called the ignition delay (TG) (13).

As the temperature increases in a reactive system, the kinetic energies of the translational motions increase and the probability of the molecules colliding with each other increases. In particular, self-ignition events arise from the autocatalytic behavior of the system, although there is no external effect (see Figure 4 for the ignition delay mechanism) (13).

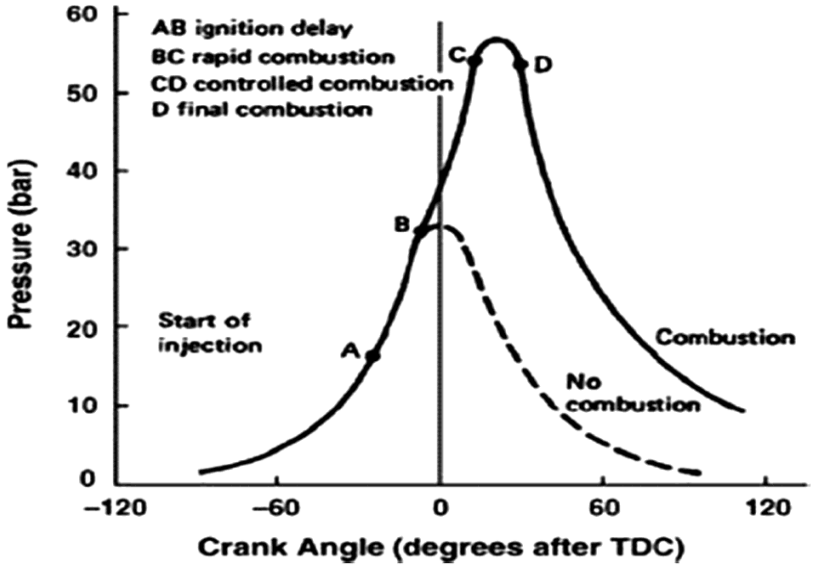

Figure 4. Ignition delay mechanism (Imdadul et al. 2015).

As can be seen in Figure 4, during fuel combustion after sparking phase, the most expected point is the U.D.P. level for the highest amount of pressure should be occurred (13, 18).

In this review, the past studies referred in the literature summarized in Table 1 (12).

The details of the studies in table are summarized in Table 2 (12).

As can be seen from Table 1, the maximum number of studies compared to the numbers before 2005 increased after 2012, reaching 52 adjectives until 2015. It is seen from this increase that the debate on increasing exhaust emissions in recent years has led to an increase in the number of such studies. As can be seen from Table 2, the Optics studies are more shallow with the maximum work done (72 pieces) depending on the knockout analysis, whereas the higher theoretical work (66 pieces) carried out in the transition to industry 4.0, mostly increases the combustion efficiency and achieves aforementioned lower emission shown in Table 1.

Table 1. The review of past studies (12).

Year	Web of Science	SAE
before 2005	111	183
2006	13	17
2007	11	13
2008	11	11
2009	17	16
2010	15	10
2011	10	8
2012	25	17
2013	31	21
2014	35	27
2015	52	28
within 2016-2017	7	12

RESULTS AND DISCUSSIONS

Fuel burning has a significant effect on the pre-ignition and high-octane burning possibilities. Most experiments in the literature show that there is no relationship between pre-ignition intensity of fuel and RON or MON. Indeed, in some experiments, the frequency of early ignition shows a further decline in the number of octanes. With the increase in the RON of the pre-ignition temperature, there is a high likelihood that the pre-flame temperature is more associated with RON and MON. However, the octane numbers (RON and MON) are particularly high, but ethanol has a relatively high tendency to premature ignition due to high intake manifold pressures. This can be explained by the fact that fuels such as ethanol and hydrogen are very sensitive to early ignition due to high laminary burning rates and lower laminary flame geometry thickness. The width of the flame of the circle in the flame center is a stable flame indicator and the flame is higher than the laminar flame. On the other hand, the tendency of ethanol fuel to be lower than gasoline fuel is due to the high ethanol evaporation temperature. In summary, pre-ignition with high octane fuel may not cause high knocking due to higher resistance to automatic ignition. As seen in Table 2, optical detection techniques, fuel properties and additives for gasoline engines can be recommended for future work.

Table 2. Details of previous studies (12).

Contents of Study	**Number**	**Topics**
Knock detection	72	1. Knock sensor development 2. Knock characterization and detection 3. Knock control logic and knock controller
Numerical simulation	68	1. The stroke model 2. Pressure oscillator modeling 3. LES model development LES model implementation delayed without ignition 4. 0-3 dimensional simulation for the 4th knockout 5. Heat transfer estimation 6. Effect of emission-type, fuel combustion conditions on the formation of combustion
Optical detection	25	1. Display of pressure waves 2. Exhaust gas automatic ignition display 3. PLIF control for HCHO estimation 4. Chemiluminescence study for intermedia products 5. Final product temperature measurement 6. Spectroscopic analysis
Theoretical study	66	1. Automatic combustion prediction 2. Hot spot auto-burn mode 3. Reaction mechanism and chemistry 4. Flame dynamics, acoustic and pressure analysis 5. Heat transfer analysis
Engine Optimization	72	1. Knock and pre-burn prevention 2. Engine operating conditions and performance
Fuel specification, Fuel additives	36	1. Octane number ratio 2. High octane fuels (alcohol, furan, NG, LPG, etc) 3. Fuel design 4. Oil additives

ACKNOWLEDGMENTS

This article partially presented as a conference proceeding of IV. Energy Efficiency Congress organized by Turkish Mechanical Engineering Board in 2017, 13-14 October, Kocaeli, Turkey. The authors are grateful to the organizers for being participated.

REFERENCES

1. Benim AC, Syed KJ. Chapter 5 - Flashback by Autoignition. Flashback Mechanisms in Lean Premixed Gas Turbine Combustion. Boston: Academic Press; 2015. p. 27-39.

2 Glassman I, Yetter RA. Chapter 7 - Ignition. Combustion (Fourth Edition). Burlington: Academic Press; 2008. p. 379-408.

3. Lifshitz A. CHAPTER 16.5 - Ignition Delay Times. Handbook of Shock Waves. Burlington: Academic Press; 2001. p. 211-VII.

4. Hidaka Y, Sato K, Henmi Y, Tanaka H, Inami K. Shock-tube and modeling study of methane pyrolysis and oxidation. Combustion and Flame. 1999;118(3):340-58.

5. Havranek T, Kokes O. Income elasticity of gasoline demand: A meta-analysis. Energy Economics. 2015;47:77-86.

6. Demirel B, Wiser WH, Oblad AG, Zmierczak W, Shabtai J. Production of high octane gasoline components by hydroprocessing of coal-derived aromatic hydrocarbons. Fuel. 1998;77(4):301-11.

7. Asinger F. CHAPTER 4 - THE MANUFACTURE OF HIGH-EFFICIENCY CARBURETTOR FUELS. Mono-Olefins: Pergamon; 1968. p. 303-413.

8. Guzzella L, Onder CH. Introduction to Modeling and Control of Internal Combustion Engine Systems: Springer; 2004.

9. Gao J, Wu Y, Shen T. Combustion Phase Control of SI Gasoline Engines Using Hypothesis Test. IFAC-PapersOnLine. 2015;48(15):153-8.

10. Heywood J. Internal Combustion Engine Fundamentals: McGraw-Hill Education; 1988.

11. Stone R. Introduction to internal combustion engines: Macmillan; 1985.

12. Wang Z, Liu H, Reitz RD. Knocking combustion in spark-ignition engines. Progress in Energy and Combustion Science. 2017;61:78-112.

13. Reif K. Gasoline Engine Management: Systems and Components: Springer Fachmedien Wiesbaden; 2014.

14. Stone R. Introduction to Internal Combustion Engines: Palgrave Macmillan; 2012.

15. Guzzella L, Onder C. Introduction to Modeling and Control of Internal Combustion Engine Systems: Springer Berlin Heidelberg; 2013.

JOTCS B
Journal of the Turkish Chemical Society
Section: B
Chemical Engineering
TURKISH CHEMICAL SOCIETY

Determining Stage Efficiency from Operating Conditions for the Liquid-Liquid Extraction Column Model Dedicated to Heavy Neutral Distillate – Aromatic Extraction Process of a Group-I Lube Base Oil Plant

Ahmet Özgür Yurdakul[1]*, Suavi Noyan Kıran[2], Oğuzhan Sağlam[2], Hamide Gürnur Odabaş[2], Begüm Avcı[3]

[1]Former member, Research and Development Center, Turkish Petroleum Refineries Corporation, Kocaeli, 41790, TURKEY
[2]Process Department, İzmir Refinery, Turkish Petroleum Refineries Corporation, İzmir, 35800, TURKEY
[3]Research and Development Center, Turkish Petroleum Refineries Corporation, Kocaeli, 41790, TURKEY

Abstract: In a lube base oil production, the feed heavy neutral distillate is originated from the fractionation of various crude oil blends. Because the changing feed properties affect both yield and quality of raffinate, the plant operating conditions need to be tuned accordingly. In this study, a predictive model for an existing industrial-scale extraction process dedicated to group-I production is constructed to determine the right operating parameters in advance, which minimizes off-spec production due to faster adaption of operation to a new feedstock. It is developed via the use of the phase equilibrium data published for heavy neutral distillate + Furfural system, laboratory measurements of physical properties and composition of distillate as well as the existing plant data. The accuracy of the corresponding process model is increased via determining stage efficiency from an empirical equation based on only selected operating conditions, namely solvent temperature and solvent-to-distillate ratio.

Keywords: Lube base oil; Aromatic extraction; Furfural; Stage efficiency; Multistage column model.

Submitted: May 15, 2018. **Accepted:** November 18, 2018.

Cite this: Yurdakul A, Kıran S, Sağlam O, Odabaş H, Avcı B. Determining Stage Efficiency from Operating Conditions for the Liquid-Liquid Extraction Column Model Dedicated to Heavy Neutral Distillate – Aromatic Extraction Process of a Group-I Lube Base Oil Plant. JOTCSB. 2018;2(1):13–36.

***Corresponding author**. **E-mail:** ahmetozguryur@yahoo.com.

INTRODUCTION

In the refining sector, different types of crude oils are blended and used as feed for their getting distilled, cracked, reformed and/or extracted into white products. On the other hand, the process units at a refinery are designed for a limited number of crude options. This sometimes causes asset loss due to capacity limitation or extended transient time for adapting the operation towards handling the crude mix to which the existing unit is unfamiliar. To eliminate, or at least, minimize the losses, it is important to have more information about the feed properties, and tools to predict the future response of the existing unit to the corresponding feed.

The Lube Base Oil (LBO) refinery units dedicated to Group-I production are based on Aromatic Extraction Process to alter the LBO Viscosity Index (VI) to the desired level. The essential information about the feed is aromatic content. The VI improvement is directly related to how much of this content is extracted from the oil via the use of a suitable solvent (S). This process is performed in an extraction column.

For a predictive model of column operation, the mathematical formulation of corresponding liquid-liquid extraction process is needed. In literature,

there is already available information on that, more specifically, the binary interaction parameters of the selected thermodynamic model equations (1–6). In the case that an equilibrium-based model is used, the stage efficiency (ε) information is required beside the phase equilibrium data, in order to represent the non-ideal stage behavior of a real column.

There are numerous studies assigning certain values for ε within the simulation process (7–10). In fact, it depends on certain parameters such as physico-chemical properties of corresponding liquid-liquid system, operating conditions such as temperature, pressure, flow rates, and mechanical design of column internals (11). Their effects on ε are examined at some degree (12, 13), and it is reported that it is difficult to estimate ε from these variables due to the complexity of the extraction process (14).

In this study, a novel and practical way of determining ε from only certain operating variables is defined. A predictive process model using the ε value calculated from these operational data is constructed for an existing aromatic extraction column operation. It is supported by the test-runs at which the existing plant operational data, as well as the feed/product quality information, are made available so that it becomes possible to fit an empirical equation based on only operating variables. It is used for estimating the product yield and quality against changing feed properties. The feed scope is kept to be Heavy Neutral Distillate (HND) for this model. The existing extraction column is simulated via use of Aspen Hysys. This Aspen model is supplemented with statistical models derived from the plant data and laboratory measurements. In this approach, data-driven models are integrated into first-principle ones, which can provide higher accuracy of performance prediction for a LBO extractive process.

MATERIALS AND EXPERIMENTAL METHODS

Bulk physical property and compositional measurements are performed for the distillate (D) samples prepared at the laboratory environment. Additional measurements are made for the selected physical properties of the distillate, raffinate (R) and extract (E) samples taken at the predetermined operational times during test-runs. The experimental procedures for all sample preparations and measurements are explained in this section.

Preparation of distillate samples

The D samples are prepared by mixing the raw R and E samples at different ratios in the laboratory. Here, the corresponding samples are provided from the existing LBO Unit of Tupras Izmir Refinery. Prior to mixing, they are heated up to 70 °C in a water bath till the samples get liquefied totally. It is followed by taking a portion of R sample into a beaker and weighed at a designated amount. The same procedure is applied to the E sample. Then, the R sample is poured into E, and stirred for a while to obtain a homogeneous mixture.

Bulk physical property measurements

Among the bulk physical properties of LBO, Total Sulfur, Carbon Residue, Density, Refractive Index and Kinematic Viscosity are measured for the D samples prepared in laboratory. Additionally, Density and Kinematic Viscosity measurements are performed for the D, R and E samples collected at the test-runs.

Total Sulfur: Energy Dispersive X-Ray Fluorescence (ED-XRF) is used to determine the total sulfur content. The instrument used for measurement is LAB X 3500 Oxford Instrument. Total sulfur analyses are performed according to IP 336 (15). Briefly, the sample is placed in the beam emitted from the X-Ray source, and the resultant excited characteristic X radiation is measured. The count (intensity) is compared with a calibration plot of counts against sulfur content as the percentage by mass. Series of calibration samples are prepared which cover the range of sulfur content of the sample. The concentration of sulfur in the sample from the calibration curve is measured by using the three average counts for each sample. The precision of the measurement is checked and approved according to the reproducibility limit given in IP 336.

Carbon Residue: The carbon residue content is determined according to ASTM D4530 (16), which provides an indication of the tendency to relative coke formation. Briefly, a weighed quantity of sample is placed in a glass vial and heated up to 500 °C under nitrogen atmosphere. Keeping at this temperature for a while, coking reactions occur and volatiles are swept away by nitrogen, simultaneously, and then the remaining carbonaceous-type residue is recorded as a percent of the original sample. The mass of the sample is selected according to ASTM D4530. It is not needed to distill the sample because of the high carbon residue results. 1.5 g +/- 0.5 g sample is directly placed to the carbon residue analyzer that is manufactured by PAC-Alcor. Two parallel experiments are performed for each sample. Precision and standard deviation of the results are checked according to ASTM D4530. The validated values are used for the examination at the modelling step.

Density: The density is measured according to EN ISO 3675 (17) by using a glass hydrometer. The values are taken at the measurement temperatures

and corrected to 15 °C (~60 °F) by means of a series of calculations and international standard tables. The sample is stirred via vertical and rotational motions to ensure uniform temperature and density through the hydrometer cylinder. The sufficient homogenate sample is transferred to the clean hydrometer cylinder to avoid the formation of air bubbles. The temperature of the sample is measured by a thermometer. It is recorded nearest 0.1 °C and the thermometer is removed, then the hydrometer is inserted for hydrometer scale reading. After reading, the hydrometer is carefully taken out of the fluid, and the thermometer is inserted again to read the temperature once more. The temperature value does not differ more than 0.05 °C from the previous reading. The quality of experimental data is checked according to the reproducibility calculation mentioned in EN ISO 3675.

Refractive Index: The refractive index is measured according to ASTM D1218 (18) by using a high-resolution refractometer of an automatic type with the prism temperature accurately controlled. The instrument used for measurement is KEM Refractometer RA-600. The sample is placed into the instrument, and the velocity of light passing through the sample fluid is measured. The refractive index is determined as the ratio of light velocity in the air to its velocity in the substance under examination. The precision for automatic digital refractive index procedure, as determined by the statistical examination, is checked for the quality of data. Accordingly, the values of RI analyses are at acceptable precision level.

Kinematic viscosity: The kinematic viscosity is determined according to EN ISO 3104 (19). The instrument used for measurement is Herzog HVM 472 viscometer. The time is measured for a fixed volume of sample fluid to flow down by gravity through a capillary tube. The kinematic viscosity is the product of measured flow time and the calibration constant of the viscometer. Two parallel measurements are made for the same sample, and the kinematic viscosity is taken as the average value of these two measurements as long as the values are within the reproducibility range.

Pseudo - Components Analyses:
The Clay-Gel absorption chromatographic method is used to determine the saturates (Satd), aromatics (Arom) and polar contents according to ASTM D2007 (20). The sample is percolated in n-pentane through a two-compartment column filled with clay and silica gel. Polar compounds are retained on the adsorbent clay while Arom are adsorbed on silica gel. Satd are not adsorbed on either clay or silica gel and collected from the bottom of the column.

As Polar compounds are retained in clay, this part is washed with 50% toluene-acetone mixture. Arom are recovered from silica gel via washing the corresponding part of column with toluene. The solvents (n-pentane, toluene, acetone) are completely removed away from the extracted fractions by using a rotary evaporator manufactured by IKA. The residuals are weighed and the pseudo-component contents are calculated accordingly. The quality of experimental data are checked against the reproducibility limits mentioned in ASTM D2007.

PROCESS DESCRIPTION

The solvent extraction unit (FEU) selectively extract the low viscosity aromatic components from the base oil stock by using furfural (furan-2-carbaldehyde) as the solvent. The feedstock of the unit is originated from the Vacuum Distillation Unit (VDU) or the Propane Deasphalting Unit (PDU). FEU has different operating modes according to the feedstock type, namely Spindle Oil (SO), Light Neutral (LN), Heavy Neutral (HN) and Bright Stock (BS). The first three are originated from VDU, while the last one comes from PDU. The main objective of the unit is to improve the Viscosity Index (VI) of the base oil. In addition to VI, oxidation stability and color stability targets are also met via extraction of poor quality aromatic compounds.

Solvent extraction unit can be divided into 4 groups (see Figure 1):

- Liquid-Liquid Extraction Section: It includes a Deaerator Tower and Rotating Disc Contactor (RDC). Deaerator tower strips Water and Air from the feed for further processing, since Water has an affinity to react with furfural. The deaerated feed enters from the bottom of the RDC while S enters from the top. S dissolves the aromatic components in the feed and the resultant extract is drawn from the bottom, while oil-rich R leaves from top of the column. Then, the products of RDC are sent to the related recovery sections.
- Raffinate & Extract Recovery Sections: Both include a Vacuum Flash Tower and Stripping Tower with necessary heating equipment.
- Furfural Drying Section: It includes a Fractionator and Dry Solvent Accumulator with necessary stripping units and heating equipment.

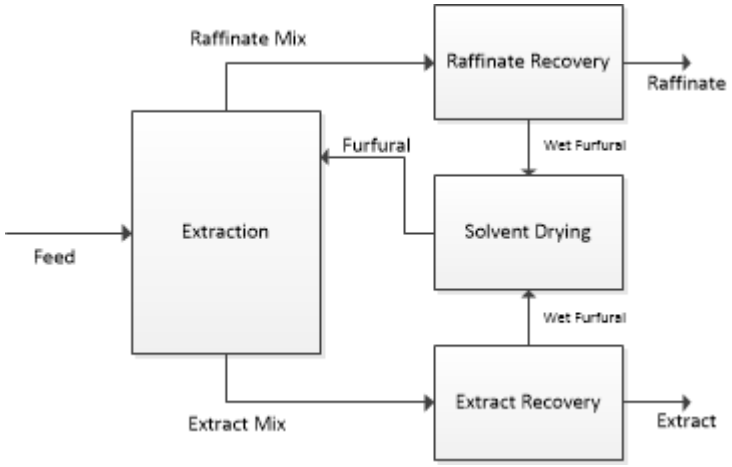

Figure 1: Solvent Extraction Unit Flowchart.

The existing Base Oil Complex is designed for Arabian light or Basra light Atmospheric Residue. The experimental crude oil is different from these.

MODEL DESCRIPTION

In the existing operation, the feed conditions are changed in daily basis due to variance in the crude mixture at the upstream. Simulating the existing extraction unit, its response to the changes in the column operating conditions, and more importantly, the bulk physical properties of the charge stream Distillate (D) can be estimated in terms of the yield and quality of the product stream R. Here, the key quality parameter for the product is Viscosity Index (VI). In the end, this model helps the Refinery Process and Planning Teams to foresee the yield and quality against changing feed conditions, which will enable better profit estimates as well as reduced amount of off-spec production during operation.

The existing industrial-scale extraction column is simulated via use of Aspen's multistage liquid-liquid extractor model. In Figure 2, the corresponding flowsheet is given. There are 3 user-defined pseudo-components representing the saturated, aromatic and polar contents of LBO. The component furfural, which corresponds to S, is also listed from the Aspen databank. The thermodynamic model is selected as NRTL for which the binary interaction coefficients published in the literature (Van Grieken et al., 2005) are used. This model is bounded to be valid for HND mode, as it is validated with the test-run data corresponding to HND. Besides NRTL parameters ae belong to Furfural extraction of HND.

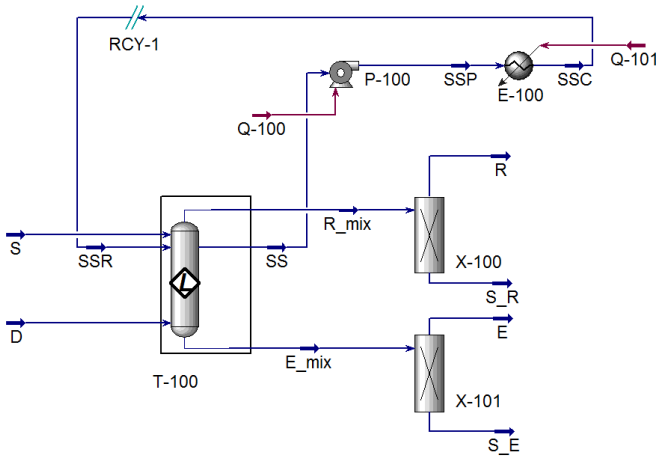

Figure 2: Aspen flowsheet of the extraction process.

In the model, D enters the column from the bottom, while S is fed from the top, representing the counter-current extraction. The bottom circulation is also added as in the case of existing unit operation. Solvent mixed R (R_mix) is taken as the top product of the column of which the bottom product is Solvent mixed Extract (E_mix). At the downstream, S is simulated to be separated from R and E at an ideal component splitter model, as the product purification and solvent recovery are not the core parts of the operation. R and E are taken from the top of splitters.

As one of the inputs to the Aspen model, the compositional data is needed for HND, so a statistical model is developed via linear regression to predict the compositions from its bulk physical properties. The expressions for the saturated and aromatic content are given in Eqs. (1) and (2), respectively.

$$x_{Satd}^{HND} = A_{0,Satd}^{HND} + \sum A_{j,Satd}^{HND} P_j^{HND} \quad \text{(Eq. 1)}$$

Where x_{Satd}^{HND}: Saturated content of HND in mass percentage

$A_{0,Satd}^{HND}$: Intercept term for saturated content estimation

$A_{j,Satd}^{HND}$: The parameter of the jth physical property of HND for saturated content

P_j^{HND}: The jth physical property of HND

$$x_{Arom}^{HND} = A_{0,Arom}^{HND} + \sum A_{j,Arom}^{HND} P_j^{HND} \quad \text{(Eq. 2)}$$

Where x_{Arom}^{HND}: Aromatic content of HND in mass percentage

$A_{0,Arom}^{HND}$: Intercept term for aromatic content estimation

$A_{j,Arom}^{HND}$: The parameter of the jth physical property of HND for aromatic content

Here, P_j corresponds to the density at 15C (d), sulfur content (SC), carbon residue (CR), refractive index (RI), the kinematic viscosity at 80 °C (KV80), and the kinematic viscosity at 100 °C (KV100).

To create a database for pseudo-component compositions as well as bulk physical properties, HND samples are prepared in the laboratory. It is done by mixing the raw raffinate and extract samples, which are collected from the existing operation, at different ratios. For each of them, pseudo-component compositions, as well as bulk physical properties, are measured. The measurement results are listed in Table 1.

As the other input to the Aspen model, a suitable value for stage efficiency needs to be assigned. For that, an empirical equation is constructed via linear regression from the operational data of the existing unit, as shown in Eq. (3).

$$\varepsilon = A_0 + \sum A_k O_k \quad \text{(Eq. 3)}$$

Where ε: Stage efficiency

A_0: Intercept term for estimation of stage efficiency

A_k: The parameter of the kth operational data of the extraction process

O_k: The kth operational data of the extraction process

Here, O_k corresponds to operational data, i.e. Distillate Temperature (T_D), Solvent Temperature (T_S), Flow rate of Distillate (F_D), Flow rate of Solvent (F_S) and Solvent-to-Distillate Flow Ratio ($F_{S/D}$).

Test-runs are performed at the existing unit to validate the complete model. The operational data of these runs, as listed in Table 2, are used for constructing the efficiency formulation. Here, the value of ε for each run is found via data reconciliation, more specifically, iterating the FR value calculated by the Aspen model to the one realized in the corresponding run.

Table 1: The lab measurements of bulk physical properties and compositions for HND samples

Sample#	d_D	SC_D	CR_D	RI_D	$KV80_D$	$KV100_D$	$Satd_D$	$Arom_D$
1	0.941	2.32	0.73	1.499	26.5	13.9	49.31	47.47
2	0.936	2.44	0.66	1.500	24.8	13.2	47.20	37.30
3	0.901	1.34	0.20	1.478	18.6	10.6	64.00	35.30
4	0.960	3.70	1.03	1.518	32.9	16.3	36.66	58.81
5	0.964	2.76	1.11	1.520	39.0	18.6	33.29	62.99
6	0.942	2.69	0.70	1.504	28.6	14.7	45.93	51.62
7	0.944	2.31	0.71	1.505	29.2	15.0	45.59	51.77
8	0.912	1.33	0.32	1.484	21.0	11.6	35.10	54.40
9	0.989	3.73	1.68	1.535	46.1	20.9	24.73	69.80
10	0.917	2.04	0.30	1.487	21.6	11.9	57.25	38.89
11	0.933	2.17	0.61	1.497	26.1	13.8	51.89	45.35
12	0.946	1.67	0.68	1.505	31.6	15.8	47.98	48.15
13	0.948	1.81	0.74	1.503	32.4	16.0	33.80	59.50
14	0.964	2.50	1.13	1.519	38.2	18.3	34.58	61.00

15	0.951	2.25	0.92	1.511	33.2	16.5	40.49	55.66
16	0.928	1.47	0.08	1.494	25.3	13.4	51.30	41.10
17	0.987	3.66	1.64	1.535	45.4	20.6	26.85	69.67
18	0.893	0.95	0.65	1.471	17.9	10.4	70.40	15.60
19	0.942	2.33	0.86	1.503	28.3	14.6	49.65	45.49
20	0.986	3.65	1.67	1.534	44.7	20.4	27.73	66.34
21	0.964	2.95	1.15	1.516	31.9	15.9	39.67	56.36
22	0.928	1.68	0.54	1.494	25.1	13.4	56.65	39.58
23	0.932	2.14	0.58	1.497	25.9	13.7	52.01	44.04
24	0.913	1.64	0.32	1.485	20.6	11.5	63.12	33.00
25	0.915	1.53	0.26	1.485	21.8	12.0	56.54	40.70
26	0.894	1.17	0.10	1.473	17.9	10.4	74.96	23.82
27	0.904	2.20	0.19	1.478	19.2	11.0	63.22	34.89
28	0.895	1.33	0.20	1.473	18.3	10.6	71.70	26.09
29	0.891	0.94	0.13	1.470	17.5	10.2	74.69	23.52
30	0.901	1.46	0.18	1.476	18.3	10.5	70.35	27.79
31	0.899	1.32	0.10	1.475	18.7	10.8	67.10	30.88
32	0.930	2.14	0.61	1.496	25.2	13.4	51.24	44.97

Table 2: Operating conditions, reconciliation ε, realized VI and composition data calculated by the Aspen model for the test-runs performed at the existing unit

TR#*	**T_D**	**T_S**	**F_D**	**F_S**	**$F_{S/D}$**	**ε**	**$Satd_R$**	**$Arom_R$**	**VI_R**
1	96.36	131.06	85.34	170.16	1.99	0.684	78.90	21.09	116.0
2	93.49	126.95	79.97	185.70	2.32	0.670	78.92	21.07	117.7
3	92.00	127.19	80.05	192.63	2.41	0.668	78.89	21.11	118.9
4	89.18	124.49	79.90	181.71	2.27	0.640	78.90	21.10	116.7
5	100.05	123.48	79.94	189.97	2.38	0.660	78.73	21.27	118.0
6	92.43	126.93	79.92	181.45	2.27	0.659	78.92	21.08	116.0
7	94.51	126.20	80.04	182.86	2.28	0.669	78.82	21.18	118.3
8	92.67	127.48	80.00	179.00	2.24	0.670	78.20	21.29	116.3
9	92.48	127.28	80.07	172.99	2.16	0.653	78.76	21.24	113.6
10	92.99	126.49	80.06	182.32	2.28	0.662	78.72	21.28	115.3
11	95.50	127.01	80.00	183.44	2.29	0.680	78.89	21.11	114.9
12	95.97	127.79	80.00	174.25	2.18	0.667	78.79	21.21	116.6
13	95.14	128.52	79.93	179.62	2.25	0.686	78.73	21.27	115.7
14	90.01	128.31	70.00	177.11	2.53	0.691	79.20	20.80	118.8
15	90.99	128.08	69.98	175.33	2.51	0.696	78.96	21.03	117.2
16	93.15	126.79	79.93	171.08	2.14	0.664	78.66	21.34	116.2
17	94.90	127.25	79.97	171.02	2.14	0.664	78.74	21.25	118.1
18	92.56	126.51	84.90	173.92	2.05	0.683	78.65	21.34	112.9
19	93.70	124.54	79.99	169.94	2.12	0.632	78.57	21.43	116.4
20	94.74	124.16	80.02	165.31	2.07	0.613	78.45	21.55	113.5
21	95.74	124.41	80.00	168.44	2.11	0.619	78.53	21.47	115.6

22	97.36	122.77	79.97	179.75	2.25	0.627	78.41	21.58	112.9
23	96.88	125.22	80.01	162.84	2.04	0.617	78.32	21.68	114.0
24	96.07	125.90	79.97	165.34	2.07	0.627	78.64	21.36	114.7

* TR: Test-run

There are 2 Aspen model outputs from which the yield and quality data can be derived: Flow rate and composition of R. The yield (Y_R) is calculated from Eq. (4).

$$Y^R = F^R/F^D \quad \text{(Eq. 4)}$$

As the key quality parameter is not the product composition but VI of R (VI_R), the compositional data calculated for R is converted into VI information via linear regression. The empirical equation is in the form given in Eq. (5).

$$VI_R = A^R_{0,VI} + A^R_{1,VI} Satd_R + A^R_{2,VI} Arom_R \quad \text{(Eq. 5)}$$

Where VI_R: Raffinate VI

$A^R_{0,VI}$: Intercept term for estimation of VI_R

$A^R_{1,VI}$: The parameter of the saturated term for VI_R

$A^R_{2,VI}$: The parameter of the aromatic term for VI_R

The compositional and VI data from the test-runs, as listed in Table 2, are used for constructing the model. Here, the compositions are found from the corresponding operational data and physical properties of feed stream via use of the Aspen model. Besides, VI_R's are calculated from the kinematic viscosity values at 40ºC (KV40) and KV100 according to ASTM D2270 (21). As the measured ones are indeed KV80 and KV100, the KV80 values need to be converted into KV40 according to the method given in ASTM D341 (22). For these transformations and calculations, the built-in software program of the viscometer is used.

Selection of the predictor variables for these 3 statistical models is discussed in the next section. Following the selection, the outliers are determined via Robust Regression. Eliminating the outliers, 75% of the operational data is used for training, and the model testing is done with the remaining 25%.

RESULTS AND DISCUSSION

Model for saturated content estimation of D

Using the data in Table 1, the linear relationship is investigated between the saturated composition and bulk physical properties of D via scattering plots, as given in Figure 3.

It is seen that the saturated content shows a smooth trend with the bulk physical properties d, RI, KV80 and KV100. As SC and CR data are rather scattered compared to the others, these are eliminated from the predictor variables. Besides, d and RI are highly correlated to each other (with Pearson product-moment correlation of 0.9970), so the only d is considered among these two to prevent bias. Together with d, the properties KV80, and KV100 are also selected as independent variables. In fact, these three selected properties require measurement time less than 1 hr, so it is also practical to use them for the prediction.

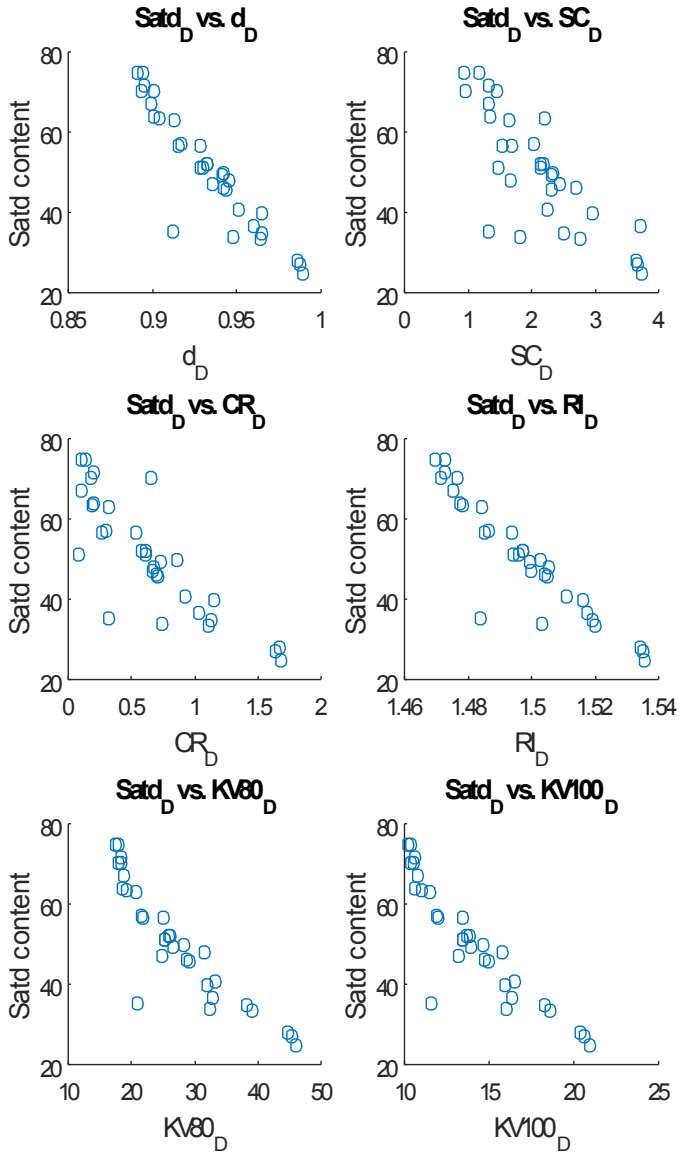

Figure 3: Scatterplots of predictor variable candidates for saturated content estimation.

Fitting a linear model with the selected predictor variables, the corresponding p-values listed in Table 3 are checked for their significance. While d_D shows its significance with a probability value lower than 0.05, KV80, and KV100 do not. It is possible that there are some outliers in the data causing this. Therefore, robust regression techniques, more specifically S estimation with 0.975 of confidence level, are applied to determine the outliers.

The outliers are found to be the 2nd, 3rd, 8th and 13th Rows. Eliminating these outliers, and using the 75% of remaining data for training, the fitting parameters are found as listed in Table 3.

Table 3: p-values for the selected bulk physical properties as predictor variables for Satd content (Values given for both complete dataset and training dataset without outliers)

	For complete dataset				For dataset without outliers			
Term	**Estimate**	**Std.Er.**	**t Ratio**	**Prob>|t|**	**Estimate**	**Std.Er.**	**t Ratio**	**Prob>|t|**
Intercept	500.92	155.1	3.23	0.0032	414.62	83.59	4.96	0.0001
d_D	-485.56	205.2	-2.37	0.0251	-336.71	111.1	-3.03	0.0075
$KV80_D$	-0.0750	2.973	-0.03	0.9800	2.9142	1.482	1.97	0.0658
$KV100_D$	0.3210	8.833	0.04	0.9713	-9.0741	4.478	-2.03	0.0587

Comparing the p-values given in Table 3, all three parameter estimates are improved after disregarding the outliers. Though the ones for KV80 and KV100 are still higher than 0.05, they are kept as the predictor variables due to the fact that the adjusted R2 increases from 0.972 to 0.975 in this case, which shows that these variables improve the model more than that would be expected by chance. Besides, one unit change of KV80 or KV100 while holding the others constant represents a non-negligible change in response. The corresponding model equation for saturated content estimation is given in Eq. (6) together with the summary of fit and ANOVA table below:

$$x_{Satd}^{HND} = 414.62 - 336.71 * d_D + 2.91 * KV80_D - 9.07 * KV100_D \quad \text{(Eq. 6)}$$

RSquare	0.979
RSquare Adj	0.975
Root Mean Square Error	2.34
Mean of Response	54.39
Observations (or Sum Wgts)	21

Source	**DF**	**Sum of Squares**	**Mean Square**	**F Ratio**
Model	3	4244.7821	1414.93	258.5350
Error	17	93.0387	5.47	**Prob > F**
C. Total	20	4337.8209		<.0001*

The model is tested with the remaining data. Putting the predicted and actual data, as well as the residual information in graphs, results in Figure 4.

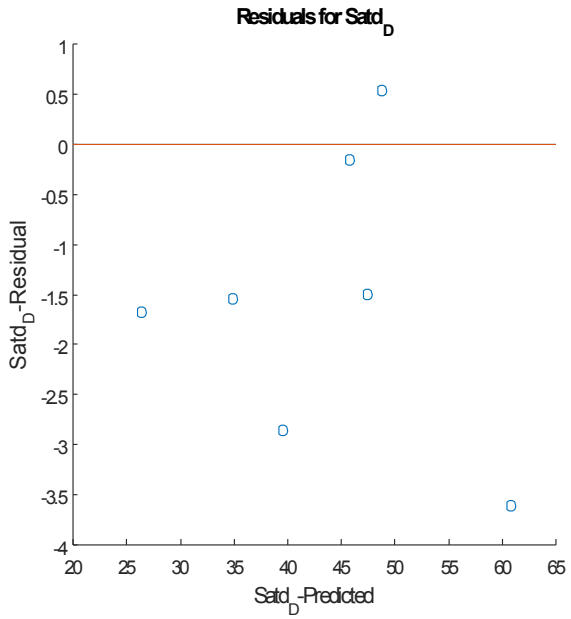

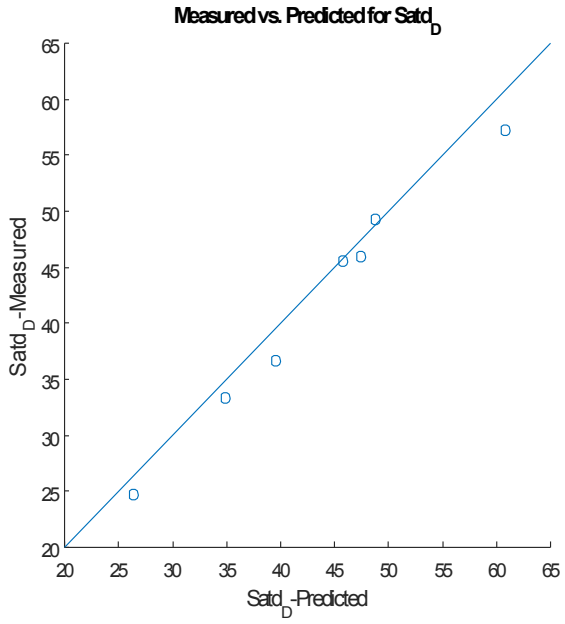

Figure 4: Plots of predicted vs. actual data (LHS) and the residual information (RHS) for saturated content estimation.

Comparing the predicted and actual data, there is a good agreement with each other. The residuals between actual data and the predicted one are varying from around -3.5 to +1 for this testing data.

Model for aromatic content estimation of D

Using the data in Table 1, the linear relationship is investigated between aromatic composition and bulk physical properties via scatter plots as given in Figure 5.

Similar to saturated one, the aromatic content shows a dependence of bulk physical properties d, RI, KV80 and KV100. As SC and CR data are rather scattered compared to the others, these are eliminated from the predictor variables. Besides, the only d is considered again among d and RI. Together with d, the properties KV80, and KV100 are selected as independent variables.

Fitting a linear model with the selected predictor variables, the corresponding p-values listed in Table 4 are checked for their significance. As those for KV80 and KV100 are far higher than 0.05, S estimation with 0.975 of confidence level is applied to determine the outliers.

The outliers are found to be the 2nd, 3rd, 8th, 13th and 18th rows (18th row is an addition compared to saturated case). Eliminating these outliers, and using the 75% of remaining data for training, the fitting parameters are found as listed in Table 4.

Table 4: p-values for the selected bulk physical properties as predictor variables for Arom content (Values given for both complete dataset and training dataset without outliers)

	For complete dataset				**For dataset without outliers**			
Term	**Estimate**	**Std.Er.**	**t Ratio**	**Prob>|t|**	**Estimate**	**Std.Er.**	**t Ratio**	**Prob>|t|**
Intercept	-310.00	142.8	-2.17	0.0386	-273.06	89.10	-3.06	0.0074
d_D	355.83	188.9	1.88	0.0701	294.26	117.6	2.50	0.0235
$KV80_D$	-0.9649	2.738	-0.35	0.7272	-2.1756	1.554	-1.40	0.1805
$KV100_D$	3.5157	8.135	0.43	0.6689	7.2443	4.679	1.55	0.1411

Comparing the p-values given in Table 4, all three parameter estimates are improved by disregarding the outliers. Though the ones for KV80 and KV100 are still higher than 0.05, they are kept as the predictor variables to value their relatively small contribution to the estimation beside the density term (R^2 is improved from 0.969 to 0.973 when viscosity terms are added into the equation.). The corresponding model equation for Aromatic content estimation is given in Eq. (7) together with the summary of fit and ANOVA table below:

$$x_{Arom}^{HND} = -273.06 + 294.26 * d_D - 2.18 * KV80_D + 7.24 * KV100_D \quad \text{(Eq. 7)}$$

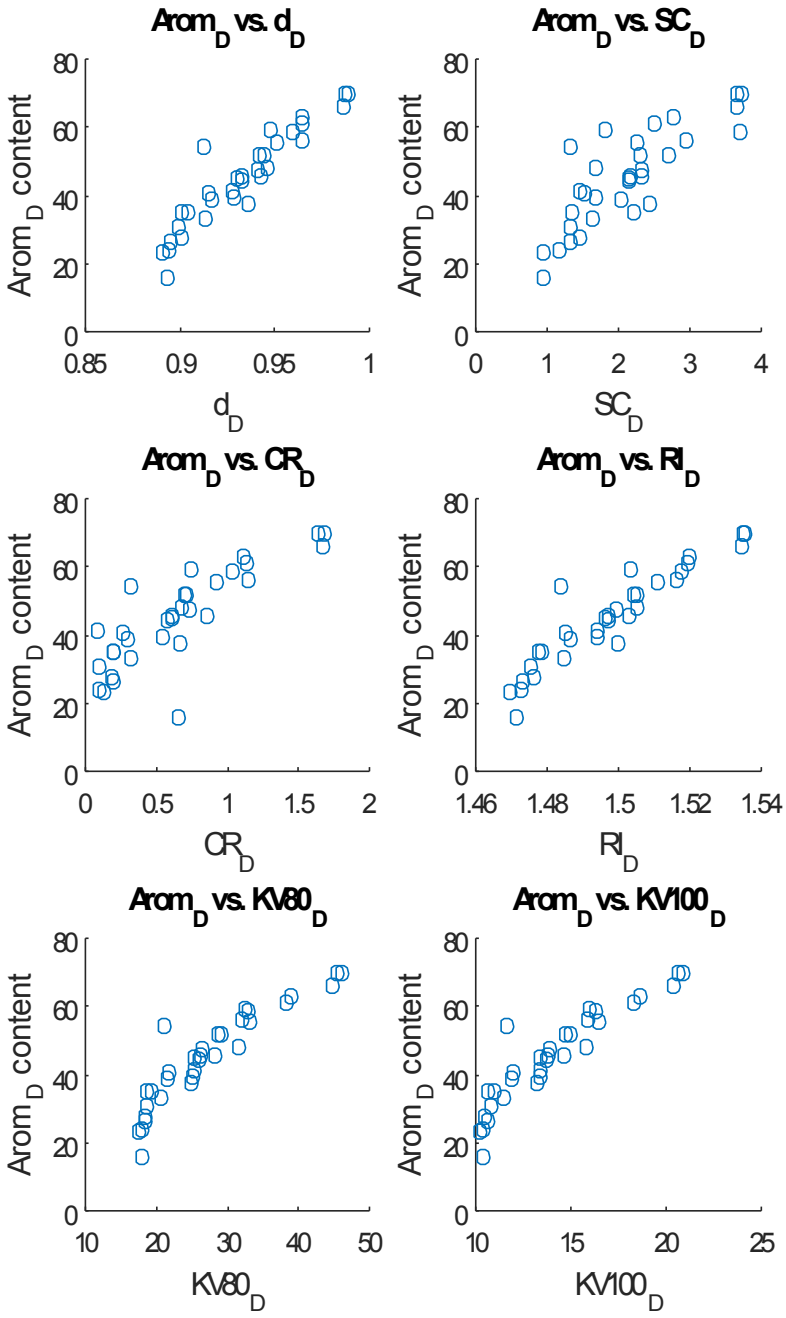

Figure 5: Scatterplots of predictor variable candidates for aromatic content estimation.

RSquare	0.973226
RSquare Adj	0.968206
Root Mean Square Error	2.440678
Mean of Response	42.92
Observations (or Sum Wgts)	20

Source	**DF**	**Sum of Squares**	**Mean Square**	**F Ratio**
Model	3	3464.4766	1154.83	193.8632
Error	16	95.3106	5.96	**Prob > F**
C. Total	19	3559.7872		<.0001*

The model is tested with the remaining data. Putting the predicted and actual data, as well as the residual information in graphs, results in Figure 6.

Comparing the predicted and actual data, there is a good agreement with each other. The residuals between actual data and the predicted one are varying from around +0.5 to +3.5 for this testing data. In other words, the prediction slightly underestimates the testing data.

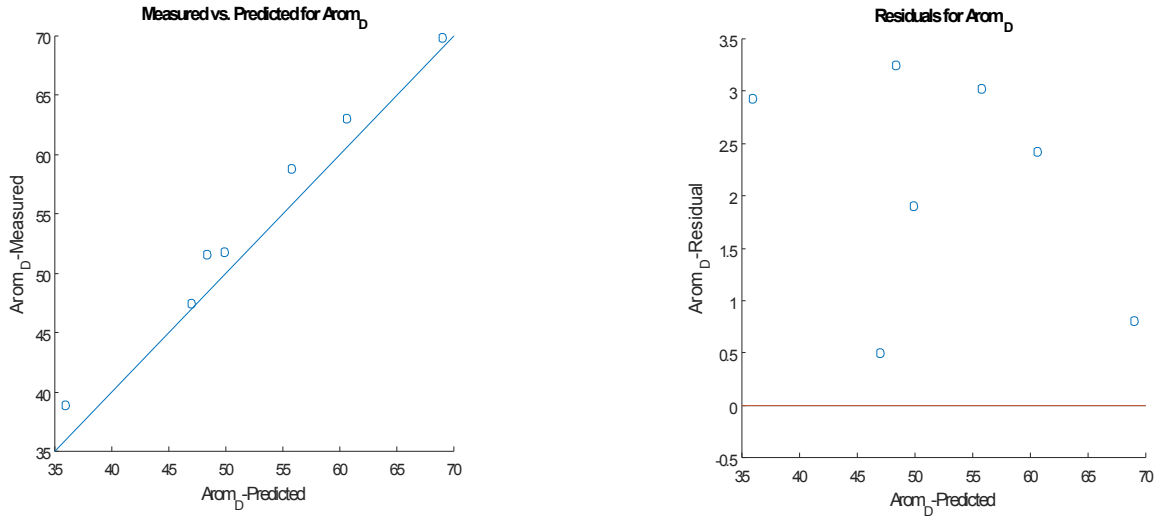

Figure 6: Plots of predicted vs. actual data supplemented (LHS) and the residual information (RHS) for aromatic content estimation.

Model for stage efficiency estimation

Using the data in Table 2, the linear relationship is investigated between stage efficiency and selected operational data via scatter plots as given in Figure 7.

Stage efficiency shows the dependence of the operational information T_S and $F_{S/D}$ with less scattered data compared to the other three variables. F_D can be treated as categorical rather than continuous data. As most of F_D is concentrated into one value for a large range of efficiency, it would not be a significant predictor. Looking at T_D and F_S, they are rather scattered. Therefore, T_S and $F_{S/D}$ are selected as significant variables.

Fitting a linear model with the selected predictor variables, the corresponding p-values listed in Table 5 are checked for their significance. As they are less than 0.05 for both variables, it is approved that they are significant for efficiency estimation. In spite of this, the calculated R^2 is 0.78, which means that only 78% of the efficiency variable is explained by the selected operational variables. It is indeed not sufficient to have results with higher accuracy from the Aspen model. Therefore, S estimation with 0.975 of confidence level is applied to determine the outliers.

The outliers are found to be the 3rd, 14th, 15th and 18th Rows. Eliminating these outliers, and using the 75% of remaining data for training, the fitting parameters are found as listed in Table 5.

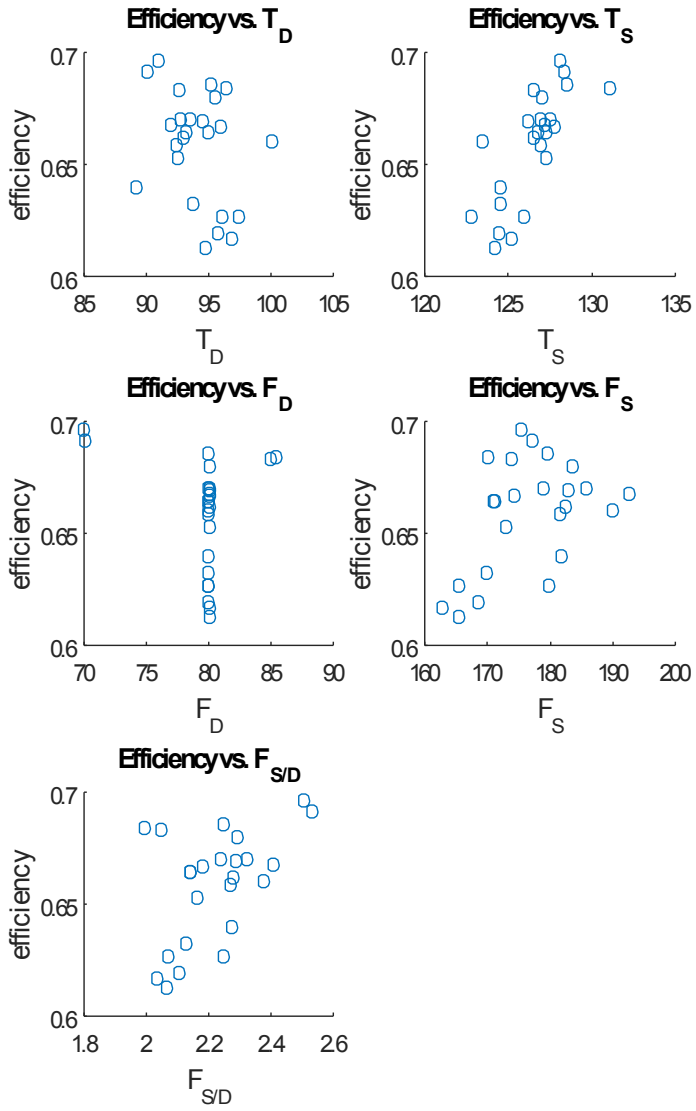

Figure 7: Scatterplots of predictor variable candidates for stage efficiency estimation.

Table 5: p-values for the selected operational data as predictor variables for efficiency (Values given for both complete dataset and the training dataset without outliers)

	For complete dataset				For dataset without outliers			
Term	**Estimate**	**Std.Er.**	**t Ratio**	**Prob>|t|**	**Estimate**	**Std.Er.**	**t Ratio**	**Prob>|t|**
Intercept	-0.7336	0.175	-4.19	0.0004	-0.9867	0.123	-8.03	<.0001
TS	0.0097	0.001	7.01	<.0001	0.0104	0.001	10.1	<.0001
FS/D	0.0771	0.018	4.34	0.0003	0.1486	0.019	7.74	<.0001

Comparing the p-values given in Table 5, disregarding the outliers makes all parameters to be much lower than 0.05. More importantly, R^2 is improved to 0.953). The corresponding model equation for stage efficiency estimation is given in Eq. (8) together with the summary of fit and ANOVA table below:

$$\varepsilon = -0.99 + 0.01 * T_S + 0.15 * F_{S/D} \text{ (Eq. 8)}$$

RSquare	0.952703
RSquare Adj	0.944821
Root Mean Square Error	0.005819
Mean of Response	0.65
Observations (or Sum Wgts)	15

Source	DF	Sum of Squares	Mean Square	F Ratio
Model	2	0.00818563	0.004093	120.8589
Error	12	0.00040637	0.000034	**Prob > F**
C. Total	14	0.00859200		<.0001*

The model is tested with the remaining data. Putting the predicted and actual data, as well as the residual information in graphs, results in Figure 8.

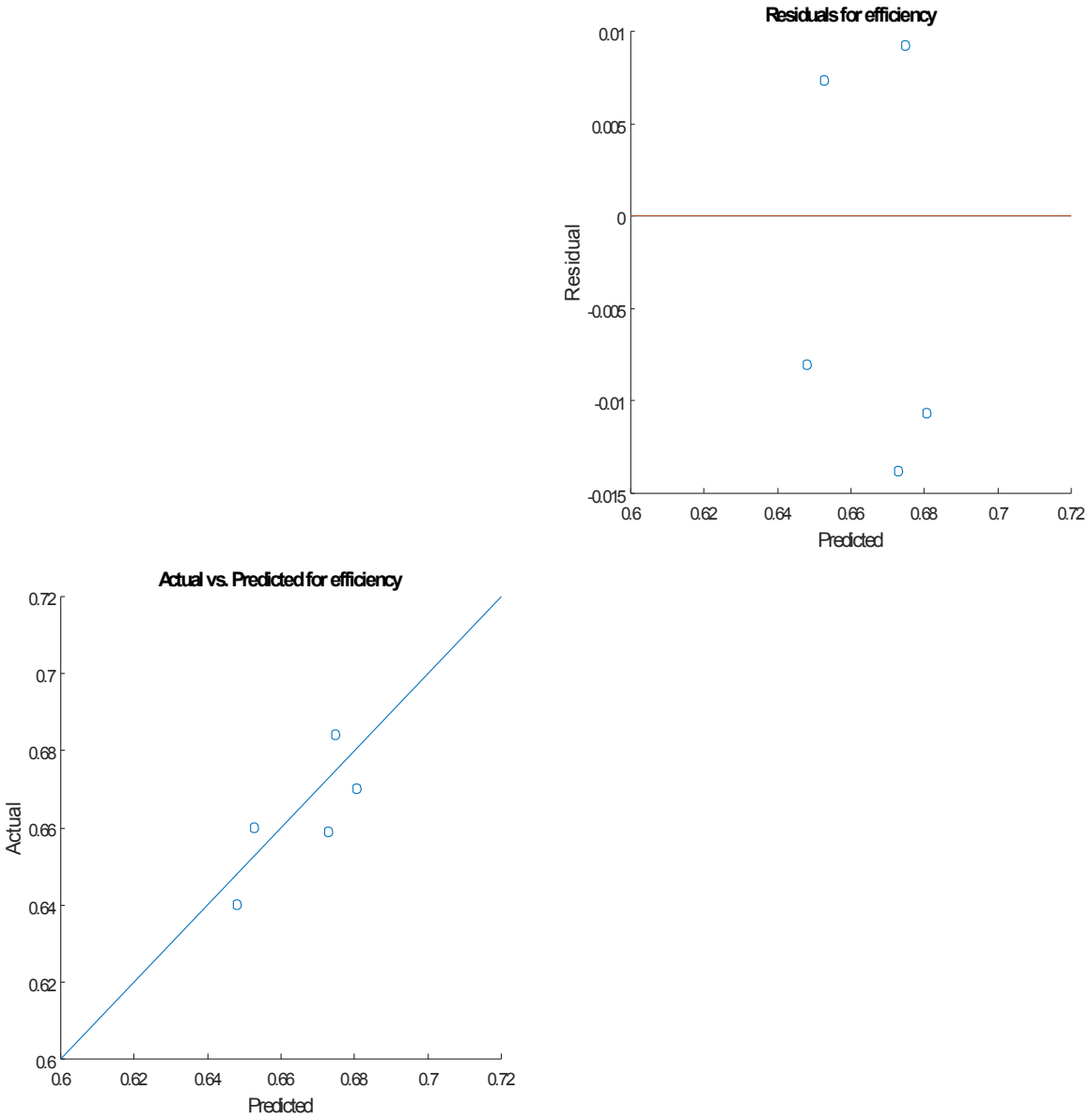

Figure 8: Plots of predicted vs. actual data (LHS) and the residual information (RHS) for stage efficiency estimation.

Comparing the predicted and actual data, there is a good agreement with each other. The residuals between actual data and the predicted one are varying from around -0.015 to +0.01 for this testing data.

Model for raffinate VI estimation

Using the data in Table 2, the linear relationship between VI_R and compositional data calculated for R by Aspen model is investigated via scatter plots, as given in Figure 9.

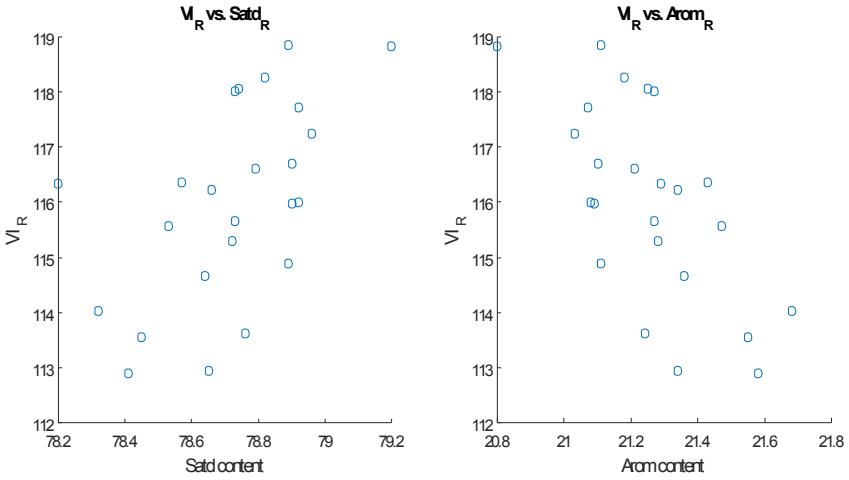

Figure 9: Scatterplots of predictor variable candidates ($Satd_R$ & $Arom_R$) for VI_R estimation.

Looking through the available data, the component values have a range of 1%, while VI_R changes in a range of 6%. Besides, the dependency is somewhat scattered.

Fitting a linear model with both saturated and aromatic contents as predictor variables, the corresponding p-values are given in Table 6. Among them, the one for aromatic content is less than 0.05, so it is kept as a predictor, while saturated content is disregarded. Here it is important to note that the calculated R^2 is only 0.44. There is also some difference between R^2 and adjusted R^2 (=0.39).

S estimation with 0.975 of confidence level is applied, but no outliers are detected with this confidence level. Using the 75% of the whole data for training, the fitting parameters are found as listed in Table 6.

Table 6: p-values for the compositional data as predictor variables for VI_R (Values given for both complete and training datasets)

	For complete dataset				**For dataset without outliers**			
Term	**Estimate**	**Std.Er.**	**t Ratio**	**Prob>|t|**	**Estimate**	**Std.Er.**	**t Ratio**	**Prob>|t|**
Intercept	344.72	284.7	1.21	0.2395	240.98	33.15	7.27	<.0001
x^R_{Satd}	-1.0152	2.820	-0.36	0.7225	0	-	-	-
x^R_{Arom}	-7.0000	3.227	-2.17	0.0417	-5.8882	1.560	-3.77	0.0017

Comparing the p-values given in Table 6, taking only the aromatic content as predictor improves the p-values. The corresponding model equation for VI_R estimation is given in Eq. (9) along with the summary of fit and ANOVA table below:

RSquare	0.470954
RSquare Adj	0.437889
Root Mean Square Error	1.264623
Mean of Response	115.8776
Observations (or Sum Wgts)	18

$$VI_R = 240.98 - 5.89 * x^R_{Arom} \quad \text{(Eq. 9)}$$

Source	**DF**	**Sum of Squares**	**Mean Square**	**F Ratio**
Model	1	22.778615	22.7786	14.2431
Error	16	25.588351	1.5993	**Prob > F**
C. Total	17	48.366966		0.0017*

Here, R^2 is improved a bit from 0.44 to 0.47 by using only aromatic content as predictor, but it is not enough to treat this model as a reliable one. This low accuracy could be originated even from the lab measurements for VI_R calculation. According to the corresponding viscosity measurement standard EN ISO 3104, the reproducibility tolerates an error of 0.65%. In the case that one viscosity value is with -0.65% error in measurement while the other one is with +0.65% error, the calculated VI (according to ASTM D2270 standard) would have an error of about 10%. For example, the VI_R calculated from the measured KV80 and KV100 for

the 20. test-run is around 113, and this can be changed from 104 to 124 by taking the error tolerance into account. Indeed, this 10% error covers the VI_R range specific to the test-run. Therefore, the equation is used as indicative, but not for decision making in operation.

In spite of low prediction power, the model is tested with the remaining data. Putting the predicted and actual data, as well as the residual information in graphs, results in Figure 10: Comparing the predicted and actual data, they are in line with each other. The residuals between actual data and the predicted one are varying from around -2.5 to +2.5 for this testing data.

Results of Yield and VI estimations via using complete model

The input and output data used for estimating Y_R and VI_R values via the complete model are given in Table 7. The measured bulk physical properties (d, KV80 and KV100) are used to calculate the composition of D, which is the input to the Aspen model. From the operational data (T_S and $F_{S/D}$), ε is found and it is again used in the Aspen model. The composition and flow rate information of R taken from the Aspen model are compared with the realized VI_R (via the lab measurements) and yield data (via the measured plant data). It is seen that data 1 & 18 for VI_R and Y_R are rather deviated from the corresponding realized ones, while the others are more in line with the real data.

Then, the predicted R_F appears to have deviated from the realized R_F at a value of -35.1%. Reminding that data 18 is determined as an outlier and disregarded during model construction for stage efficiency, such deviation in the predicted values corresponding to this data is reasonable. Comparing the data for row 18 with 17, the physical properties of HND (d_D, $KV80_D$ and $KV100_D$) are quite close to each other. It is an expected result for feed properties, as 18. Run is indeed subsequent to 17 within the same operational day. The operational data used for ε prediction are slightly different which causes a difference in the value of ε. However, these differences would not cause such deviation in the prediction power of i.e. Y_R for run 18 compared to 17. In fact, it is the result of fluctuation in the realized raffinate flow of run 18, as seen from Figure 11. The interquartile of F_R is wider for run 18. With whisker length being 1.0 times the interquartile range, there are 3 outliers for run 18, while there is only one for run 17. This results in higher average R_F and so higher reconciliation efficiency value than it should be for data 18.

The other deviated one, data 1, is indeed not used in model construction at all. It remained in the testing part, so its deviation is detected at this later stage. Looking through the details from Table 7, the physical properties and composition data are in line with each other. However, as it is seen from Figure 12, there is a fluctuation especially in F_S and T_S at the time span between 40 and 60. This causes deviation in the average values of F_S and T_S which are used in ε prediction. Eventually, it brings the corresponding error in the predicted Y_R value.

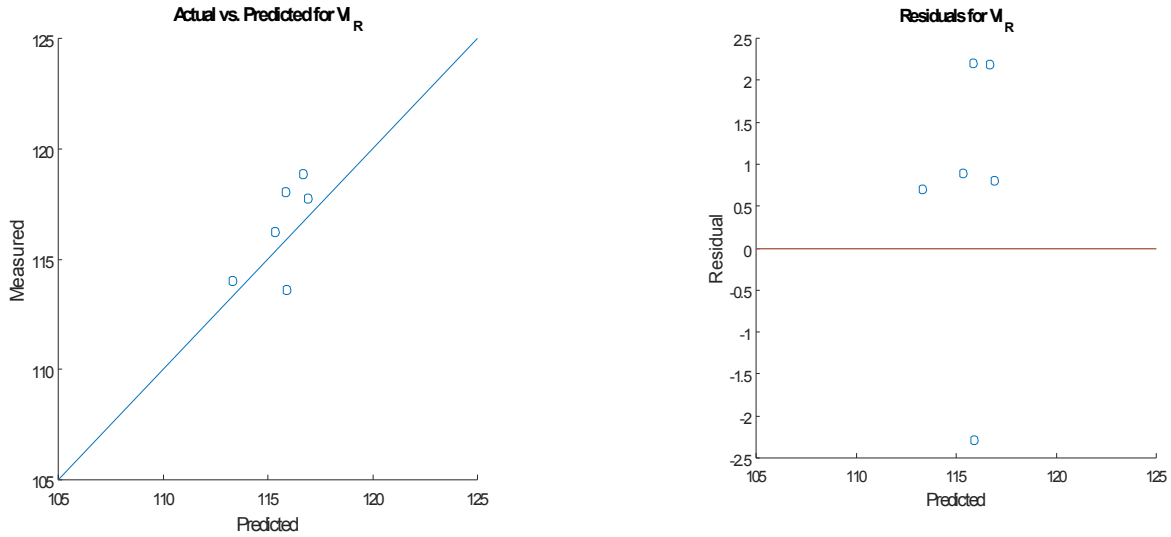

Figure 10: Plots of Predicted vs. actual data (LHS) and the residual information (RHS) for VI_R estimation.

Table 9: The realized operational & experimental data and model results for the additional test-runs

Lab measurements	Model	Op. data	ε	Model	VI_R	Y_R

d_D	KV80 D	KV100 D	Satd D	Arom D	T_S	$F_{S/D}$	Model	Satd R	Arom R	ASTM	Model	Error %	Op.	Model	Error %
0.936	25.40	13.40	51.99	44.09	122.69	2.16	0.612	78.12	21.88	108.7	112.1	3.2	0.51	0.47	-7.7
0.935	25.24	13.33	52.49	43.64	126.03	2.16	0.647	78.28	21.71	110.5	113.1	2.4	0.48	0.47	-3.8
0.935	25.40	13.41	52.20	43.90	126.70	2.13	0.650	78.30	21.70	110.3	113.2	2.6	0.46	0.47	2.8
0.938	25.98	13.60	50.95	45.07	124.62	2.21	0.639	78.42	21.58	108.9	113.9	4.6	0.42	0.46	8.0
0.939	25.99	13.57	51.15	44.93	125.63	2.19	0.647	78.27	21.73	112.4	113.0	0.5	0.43	0.48	11.9
0.940	26.23	13.68	50.32	45.67	125.70	2.22	0.653	78.72	21.28	115.1	115.7	0.5	0.40	0.42	4.9
0.940	26.14	13.63	50.71	45.33	125.94	2.24	0.658	78.51	21.49	110.7	114.4	3.4	0.41	0.42	4.6
0.940	26.23	13.67	50.41	45.60	127.12	2.28	0.676	78.85	21.15	113.0	116.4	3.0	0.37	0.42	12.0
0.940	26.10	13.62	50.48	45.52	127.13	2.31	0.681	78.68	21.32	114.0	115.4	1.3	0.37	0.43	16.6

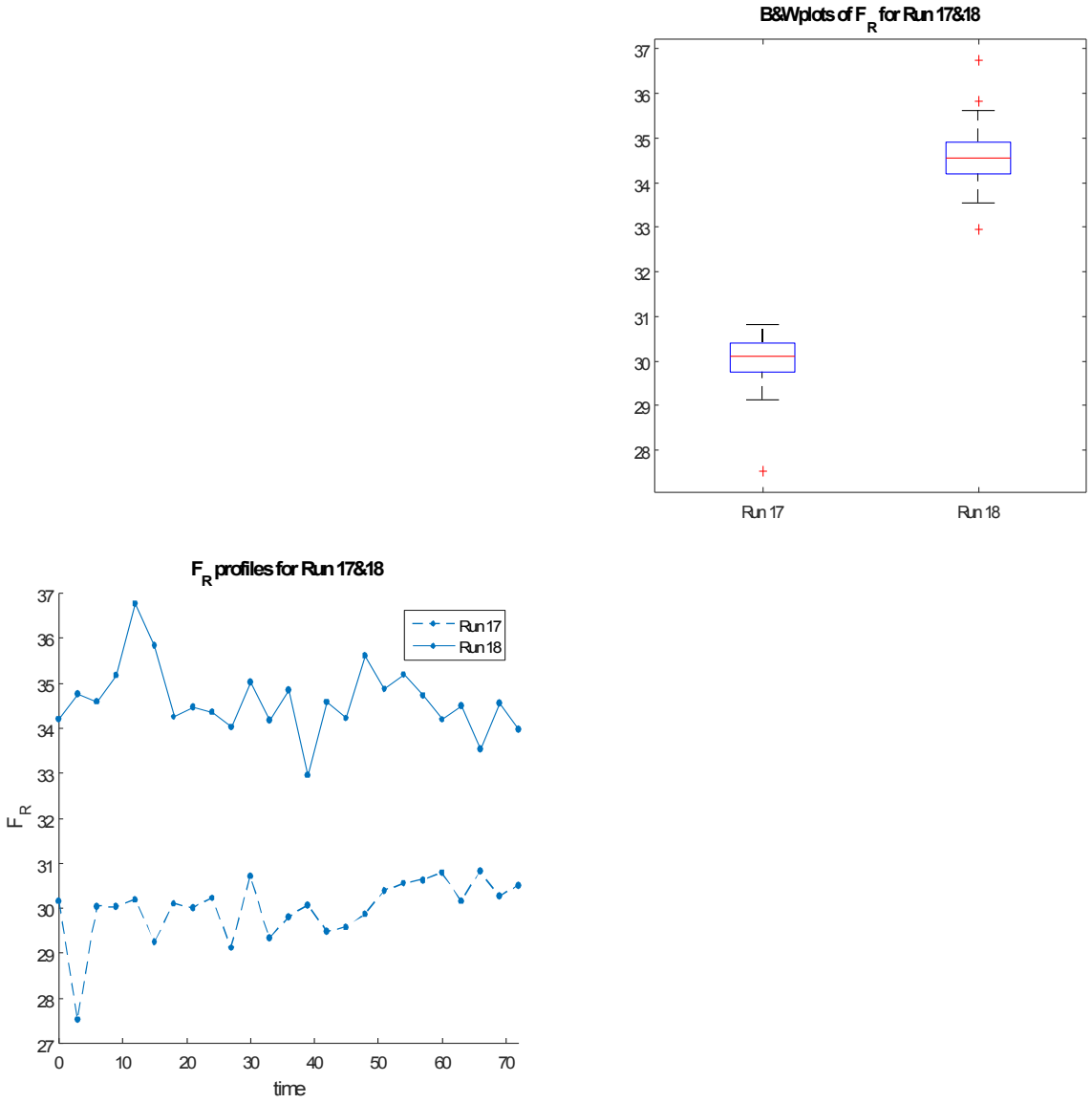

Figure 11: Plots of F_R profiles in a timespan (LHS) and Box & Whisker (RHS) corresponding to Run 17 & 18.

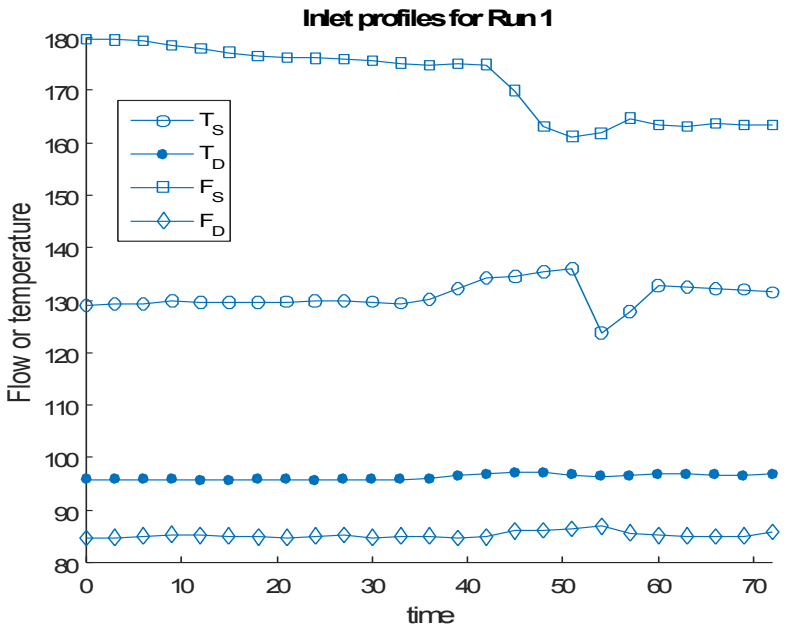

Figure 12: Operational profiles in a timespan corresponding to Data 1.

Along with data 1 and 18, RMSE is calculated to be 1.7 and 0.047 for VI_R and Y_R, respectively. Extracting these 2 outliers, the RMSE decreases to 1.3 and 0.031, respectively. These values are at acceptable levels, so the model can be used for prediction of VI_R and Y_R via using only the measured bulk physical properties of distillate together with the operational data already available in the plant historian. In addition to that, Y_R prediction can be used for decisive actions, such as tuning of operating conditions and profit maximization.

Estimating ε from the selected inlet operating conditions gives higher accuracy of model compared to use of a constant value for all operating conditions. The results are given for comparison in Table 8. Here, the constant value of ε is taken as the average of reconciliations from Table 2. The rows belonging to Run 1 and 18 are extracted from this table. Calculating the RMSE values for both the model predicted F_R's and those found by keeping ε constant at 0.658, they are found as 2.4 and 6.0, respectively. This shows that the power of prediction increases when the hydraulic changes are taken into account at each run.

Table 8: The realized and model predicted F_R values beside the calculated F_R with constant ε

TR#	F_R (realized)	F_R (model)	Error%*	F_R (ε=0.658)	Error%**
2	29.64	32.43	9.4	25.91	-12.6
3	29.24	34.69	18.6	26.27	-10.2
4	30.47	32.36	6.2	34.36	12.8
5	35.12	34.22	-2.6	34.85	-0.8
6	31.57	34.68	9.9	31.53	-0.1
7	32.58	32.11	-1.4	30.10	-7.6
8	30.72	31.93	4.0	27.13	-11.7
9	32.01	33.79	5.6	33.22	3.8
10	31.44	33.05	5.1	30.46	-3.1
11	32.04	31.65	-1.2	26.04	-18.7
12	29.34	29.91	1.9	26.52	-9.6
13	31.97	32.09	0.4	23.04	-27.9
14	27.22	31.56	16.0	19.89	-26.9
15	28.60	31.51	10.2	21.00	-26.6

16	31.35	26.30	-16.1	29.34	-6.4
17	30.09	27.00	-10.3	27.75	-7.8
19	33.65	32.15	-4.4	38.47	14.3
20	32.41	32.38	-0.1	40.45	24.8
21	33.83	34.50	2.0	40.64	20.1
22	36.19	36.03	-0.5	40.71	12.5
23	33.31	34.27	2.9	41.45	24.5
24	32.03	33.43	4.4	38.88	21.4

* Corresponding to the model calculated efficiency
** Corresponding to the constant value of efficiency

Table 7: Input and output data for model estimation of VI_R and Y_R

	Lab measurements					Op. data		ε	Model	VI_R				Y_R		
TR#	**d_D**	**$KV80_D$**	**$KV100_D$**	**$Satd_D$**	**$Arom_D$**	**TS**	**$F_{S/D}$**	**Model**	**$Satd_R$**	**$Arom_R$**	**ASTM***	**Model**	**Error%**	**Op.**	**Model**	**Error%**
1	0.936	25.55	13.37	52.53	43.70	131.06	1.99	0.675	78.90	21.09	116.0	119.7	3.2	0.33	0.23	-31.3
2	0.938	25.72	13.52	51.06	44.94	126.95	2.32	0.681	78.92	21.07	117.7	117.3	-0.4	0.37	0.41	9.4
3	0.938	25.58	13.42	51.49	44.58	127.19	2.41	0.696	78.89	21.11	118.9	116.4	-2.1	0.37	0.43	18.6
4	0.939	25.74	13.55	50.61	45.32	124.49	2.27	0.648	78.90	21.10	116.7	116.1	-0.5	0.38	0.41	6.2
5	0.939	25.54	13.39	51.48	44.60	123.48	2.38	0.653	78.73	21.27	118.0	115.7	-1.9	0.44	0.43	-2.6
6	0.939	25.81	13.50	51.06	44.98	126.93	2.27	0.673	78.92	21.08	116.0	115.6	-0.3	0.40	0.43	9.9
7	0.939	25.86	13.52	51.03	45.02	126.20	2.28	0.667	78.82	21.18	118.3	116.9	-1.2	0.41	0.40	-1.4
8	0.940	26.08	13.61	50.78	45.25	127.48	2.24	0.674	78.20	21.29	116.3	115.9	-0.3	0.38	0.40	4.0
9	0.940	26.15	13.64	50.68	45.35	127.28	2.16	0.660	78.76	21.24	113.6	114.6	0.8	0.40	0.42	5.6
10	0.938	26.21	13.67	50.99	45.08	126.49	2.28	0.669	78.72	21.28	115.3	115.6	0.3	0.39	0.41	5.1
11	0.939	26.12	13.66	50.62	45.38	127.01	2.29	0.677	78.89	21.11	114.9	116.6	1.4	0.40	0.40	-1.2
12	0.939	26.20	13.67	50.66	45.37	127.79	2.18	0.668	78.79	21.21	116.6	117.2	0.5	0.37	0.37	1.9
13	0.939	26.15	13.65	50.69	45.33	128.52	2.25	0.686	78.73	21.27	115.7	115.7	0.0	0.40	0.40	0.4
14	0.940	26.15	13.68	50.12	45.81	128.31	2.53	0.726	79.20	20.80	118.8	116.2	-2.2	0.39	0.45	16.0
15	0.940	26.22	13.69	50.20	45.76	128.08	2.51	0.720	78.96	21.03	117.2	115.7	-1.2	0.41	0.45	10.2
16	0.938	25.66	13.50	51.23	44.78	126.79	2.14	0.652	78.66	21.34	116.2	117.6	1.2	0.39	0.33	-16.1
17	0.937	25.72	13.51	51.52	44.55	127.25	2.14	0.656	78.74	21.25	118.1	118.4	0.3	0.38	0.34	-10.3
18	0.937	25.75	13.67	50.19	45.61	126.51	2.05	0.635	78.65	21.34	112.9	117.6	4.1	0.41	0.26	-35.1
19	0.938	25.55	13.44	51.29	44.73	124.54	2.12	0.626	78.57	21.43	116.4	114.3	-1.8	0.42	0.40	-4.4
20	0.938	25.60	13.46	51.18	44.83	124.16	2.07	0.613	78.45	21.55	113.5	114.1	0.5	0.41	0.40	-0.1
21	0.936	25.04	13.22	52.44	43.69	124.41	2.11	0.622	78.53	21.47	115.6	113.9	-1.5	0.42	0.43	2.0
22	0.936	25.04	13.22	52.37	43.75	122.77	2.25	0.626	78.41	21.58	112.9	114.0	0.9	0.45	0.45	-0.5
23	0.936	24.97	13.18	52.53	43.61	125.22	2.04	0.620	78.32	21.68	114.0	113.7	-0.3	0.42	0.43	2.9
24	0.937	25.12	13.24	52.32	43.81	125.90	2.07	0.632	78.64	21.36	114.7	114.4	-0.3	0.40	0.42	4.4

* According to ASTM D2270

A second validation is performed for the model by conducting an additional series of test-runs at the existing unit. The realized operational and experimental data together with the model results are given in Table 9. Accordingly, the percent errors for Y_R vary between -7.7 and 16.6, while those for VI_R are up to 14%. The plots of predicted vs. realized data and the residuals are also given in Figures 13 & 14.

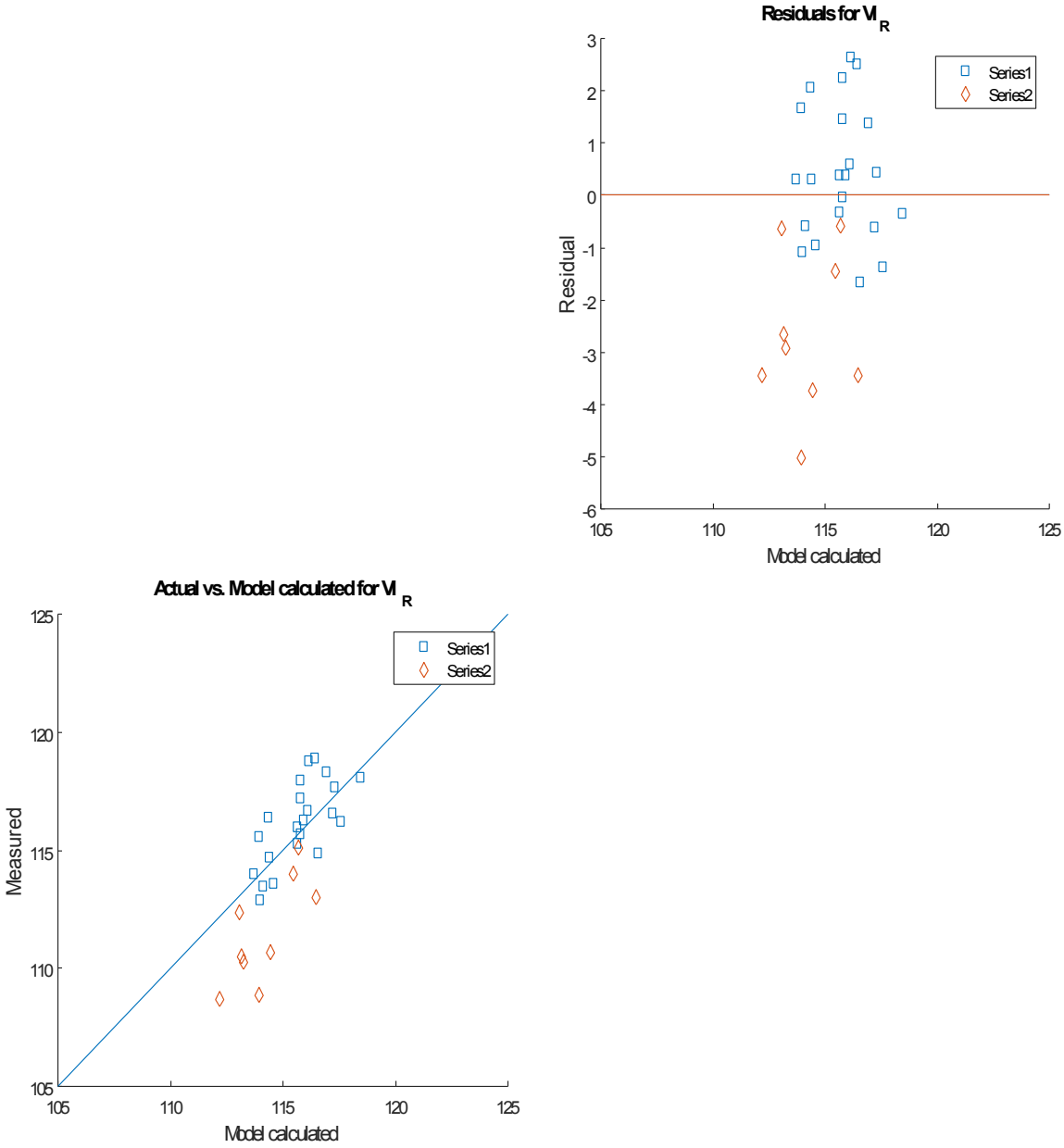

Figure 13: Plots of predicted vs. realized data (LHS) and the residuals (RHS) for VI_R prediction.

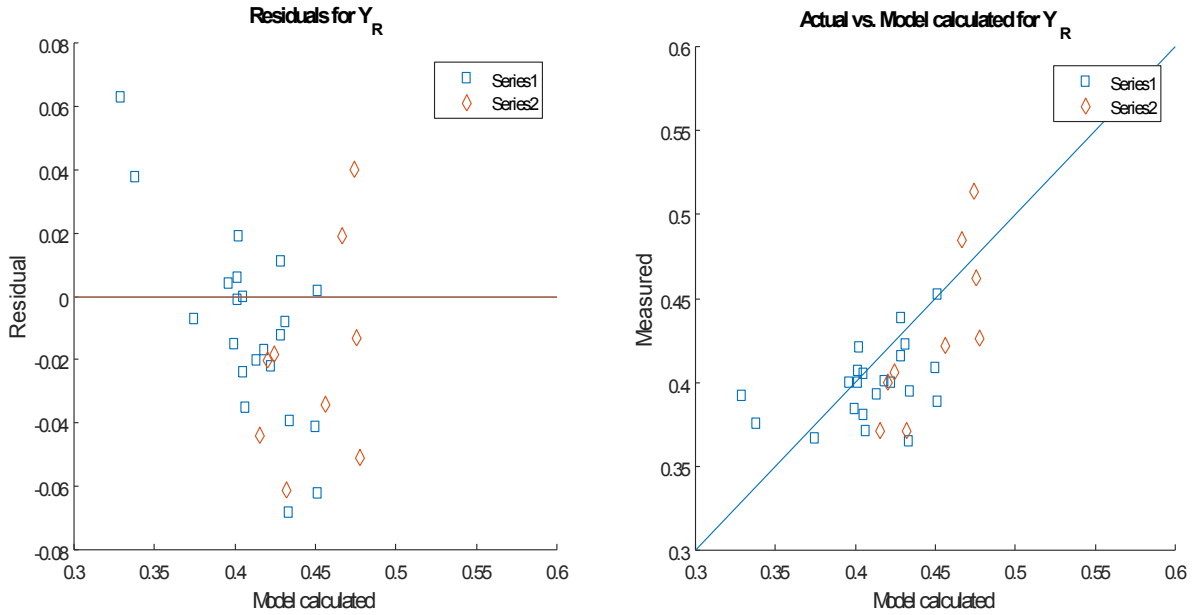

Figure 14: Plots of predicted vs. realized data (LHS) and the residuals (RHS) for Y_R prediction.

The model overpredicts VI_R values for this dataset. The RMSE for VI_R values is calculated as 3. Referring to the previously stated uncertainty in VI values originated from the lab measurements, these results prove that VI_R prediction should be kept as the indication only. For Y_R, RMSE is 0.04, which is an acceptable level.

CONCLUSION

The test-runs conducted in the existing lube base oil unit validate that Aspen process model supported with a regression model for stage efficiency has a higher accuracy compared to the one for which the efficiency is a constant value. This shows that the prediction power can be increased by taking the hydraulic changes into account at each run.

The published phase equilibrium data for Heavy Neutral Distillate + Furfural system is used for constructing the industrial-scale extraction process model in Aspen Hysys. Here, the distillate is composed of three pseudo-components; namely saturated, aromatic and polar. The compositional data (as an input of feed stream in the process model) is determined from the bulk physical properties of distillate. Applying multiple regression techniques to the laboratory data, density as well as kinematic viscosity at 80 and 100 °C are found to be significant predictors for saturated and aromatic compositions. Refractive index shows significance but it is highly correlated with density as well. Sulfur content and carbon residue values are rather scattered considering the measured values of compositions.

As another input for Aspen model, the stage efficiency is calculated from the operating conditions. Analyzing the corresponding test-run data, the solvent temperature and solvent-to-distillate ratio have significance for predicting the efficiency value.

Raffinate yield and VI are the key performance parameters for the extraction process. Raffinate flow rate and composition data is available as Aspen model output. Yield is calculated as raffinate-to-distillate flow ratio. To obtain VI value, the composition data from Aspen model is converted into VI via a statistical model which is constructed by using test-run data from the existing plant. As the composition data used for model construction has a narrow range (1%), the VI prediction can be used for only indication. On the other hand, yield prediction has a fair accuracy with relative error changing between -16 to +19%, and it can be used for decision making by the corresponding process and planning teams of the refinery.

ACKNOWLEDGMENTS

This work was partially supported by Scientific and Technological Research Council of Turkey grant funded by Turkish government (TEYDEP project number: 3130749).

NOMENCLATURE

A_0: Intercept term for estimation of stage efficiency
$A_{0,Arom}^{HND}$: Intercept term for aromatic content estimation
$A_{0,satd}^{HND}$: Intercept term for saturated content estimation

$A_{j,Arom}^{HND}$: The parameter of the jth physical property of HND for aromatic content
$A_{j,satd}^{HND}$: The parameter corresponding to the jth physical property of HND
A_k : The parameter of the kth operational data of extraction process
Arom: Aromatic content
BLO: Base Lube Oil
BS: Bright Stock
CR: Carbon Residue
d: Density@15C
D: Distillate
ε: Stage efficiency
E_mix: Extract mixed with Solvent
F: Operational flowrate
FEU: Solvent (Furfural) Extraction Unit
HN: Heavy Neautral
HND: Heavy Neutral Distillate
KV40: Kinematic viscosity at 40C
KV80: Kinematic viscosity at 80C
KV100: Kinematic viscosity at 100C
LN: Light Neutral
O_k: The kth operational data of extraction process
P_j^{HND}: The jth physical property of HND
PDU: Propane Deasphalting Unit
R: Raffinate
R_mix: Raffinate mixed with Solvent
RDC: Rotating Disc Column
RI: Refractive Index
RMSE: Root Mean Square Error
S: Aromatic extracting solvent
Satd: saturated content
SC: Sulfur content
SO: Spindle Oil
T: Operational temperature
VDU: Vacuum Distillation Unit
VI: Viscosity Index
x_{Arom}^{HND}: Aromatic content of HND in mass percentage
x_{Satd}^{HND}: Saturated content of HND in mass percentage
Y: Yield

REFERENCES

1. Espada JJ, Coto B, Romero R van, Moreno JM. Simulation of pilot-plant extraction experiments to reduce the aromatic content from lubricating oils. Chemical Engineering and Processing. 2008;(47):1398–403.

2. Coto B, Grieken R van, Pena JL, Espada JJ. A model to predict physical properties for light lubricating oils and its application to the extraction process by furfural. Chemical Engineering Science. 2006;(61):4381–92.

3. Coto B, Grieken R van, Pena JL, Espada JJ. A generalized model to predict the liquid-liquid equilibrium in the systems furfural + lubricating oils. Chemical Engineering Science. 2006;(61):8028–39.

4. Grieken R van, Coto B, Romero E, Espada JJ. Prediction of Liquid-Liquid Equilibrium in the System Furfural + Heavy Neutral Distillate Lubricating Oil. 2005;(44):8106–12.

5. Grieken R van, Coto B, Pena JL, Espada JJ. Application of a generalized model to the estimation of physical properties and description of the aromatic extraction from a highly paraffinic lubricating oil. Chemical Engineering Science. 2008;(63):711–20.

6. Espada JJ, Coto B, Pena JL. Liquid-liquid equilibrium in the systems furfural + light lubricating oils using UNIFAC. Fluid Phase Equilibria. 2007;(259):201–9.

7. Pashikanti K, Liu YA. Predictive Modeling of Large-Scale Integrated Refinery Reaction and Fractionation Systems from Plant Data. Part 3: Continuous Catalyst Regeneration (CCR) Reforming Process. Energy Fuel. 2011;(25):5320–44.

8. Albahri TA. Molecularly Explicit Characterization Model (MECM) for Light Petroleum Fractions. Ind Eng Chem Res. 2005;(44):9286–98.

9. Ferreira MC, Meirelles AJA, Batista EAC. Study of the Fusel Oil Distillation Process. Ind Eng Chem Res. 2013;(52):2336–51.

10. Yang C, Yang S, Qian Y, Guo J, Chen Y. Simulation and Operation Cost Estimate for Phenol Extraction and Solvent Recovery Process of Coal-Gasification Wastewater. Ind Eng Chem Res. 2013;(52):12108–15.

11. Muhammad A, GadelHak Y. Correlating the additional amine sweetening cost to acid gases load in natural gas using Aspen Hysys. J of Natural Gas Sci and Eng. 2014;(17):119–30.

12. Maldonado EQ, Meindersma GW, Haan AB. Ionic

liquid effects on mass transfer efficiency in extractive distillation of water-ethanol mixtures. Computers and Chemical Engineering. 2014;(71):210–9.

13. Singh D, Gupta RK, Kumar V. Simulation of a plant scale reactive distillation column for esterification of acetic acid. Computers and Chemical Engineering. 2015;(73):70–81.

14. Mehrkesh A, Tavakoli T, Hatamipour MS, Karunanithi T. Modeling and Simulation of a Rotating-Disk Contactor for the Extraction of Aromatic Hydrocarbons from a Lube-Oil Cut. Ind Eng Chem Res. 2013;(52):9422–32.
15. IP 336/04: Petroleum products – Determination of sulfur content – Energy-dispersive X-ray fluorescence spectrometry (ISO 8754:2003). CEN; 2014.

16. ASTM D4530-11: Standard Test Method for Determination of Carbon Residue (Micro Method). ASTM International; 2011.

17. TS 1013 EN ISO 3675: Crude petroleum and liquid petroleum products – Laboratory determination of density or relative density – Hydrometer method. TSE; 2002.

18. ASTM D1218-12: Standard Test Method for Refractive Index and Refractive Dispersion of Hydrocarbon Liquids. ASTM International; 2016.

19. TS 1451 EN ISO 3104: Petroleum products – Transparent and opaque liquids – Determination of kinematic viscosity and calculation of dynamic viscosity (ISO 3104). TSE; 1999.

20. ASTM D2007-11: Standard test method for Characteristic Groups in Rubber Extender and Processing Oils and Other Petroleum-Derived Oils by the Clay-Gel Absorption Chromatographic Method. ASTM International; 2011.

21. ASTM D2270-10: Standard Practice for Calculating Viscosity Index from Kinematic Viscosity at 40°C and 100°C. ASTM International; 2009.

22. ASTM D341-09: Standard Practice for Viscosity-Temperature Charts for Liquid Petroleum Products. ASTM International; 2009.

JOTCS B
Journal of the Turkish Chemical Society
Section: B
Chemical Engineering
TURKISH CHEMICAL SOCIETY

The Production and Characterization of Activated Carbon Using Pistachio Shell through Carbonization and CO_2 Activation

İlhan Küçük[a], Yunus Önal[b*], Canan Akmil-Başar[b]

[a] Department of Chemistry, Faculty of Art and Science, Inonu University, 44280 Malatya, Turkey
[b] Department of Chemical Engineering, Faculty of Engineering, Inonu University, 44280 Malatya, Turkey

Abstract: In this study, activated carbon from pistachio shell has been successfully produced through carbonization and CO_2 activation. The pistachio shell has been carbonized at 300, 400, 500, 600, 700, 800, 900, and 1000 °C temperature, and 100 and 500 mL / min inert nitrogen atmosphere. Char, liquid and gas yields have been investigated during the carbonization process. In the carbonization, generally the solid yield decreases as the temperature increases, while the gas efficiency increases. The increase in liquid yield was lower than the gas yield. Carbonized samples were subjected to physical activation with carbon dioxide at a flow rate of 100 mL / min at 800 °C and 900 °C. As a result of carbon dioxide activation, BET surface area values were obtained in the range of 16.66-857.13 m^2 / g. The highest surface area was obtained as 857.13 m^2 / g. at 600 °C carbonization temperature, 100 mL / min nitrogen flow rate and 800 °C activation temperature 100 mL / min carbon dioxide flow rate. The mean pore diameter values of the activated carbon samples were measured in the range of 2.07-4.06 nm. The average pore size distribution of some of the samples is in a relatively narrow range and is mostly of molecular sieve size in nano pore size. According to the XRD results, all samples were found to be amorphous.

Keywords: Biomass, carbonization, physical activation, activated carbon.

Submitted: November 07, 2018. **Accepted:** February 28, 2019.

Cite this: Küçük İ, Önal Y, Akmil-Başar C. The Production and Characterization of Activated Carbon Using Pistachio Shell through Carbonization and CO2 Activation. JOTCSB. 2019;2(1): 35–44.

***Corresponding author. E-mail:** yunus.onal@inonu.edu.tr.

INTRODUCTION

Increasing industrialization brings the population to cities and as a result, it brings water and air pollution to a great extent. Due to the increase in the consumption of metropolises, the diversity of pollutants is greatly increasing. As a result of this increase, especially the contamination concentrations of the aqueous media are large. Pollution is in domestic and industrial wastewater, thrown into the environment by mixing with rain and snow water from the soil. Therefore, the treatment of water in the treatment plants alone cannot solve the pollution problem. The concentration of pollutants, especially drugs used for humans and animals, increases rapidly. Apart from this, in order to meet the increasing food needs of people, the use of pesticides as a result of agriculture is also an important pollution. The chemicals that are mixed in the soil, pollute the ground water from here and the underground waters reach the lakes and seas by the streams. The pesticide and herbicides used are halogen-derived and the capacity to form a large number of new compounds in the natural environment increases the pollution (1).

In addition to this pollution, air pollution, which is another problem of the increasing world population, is also important for years. In particular, the growth of cities and the advancement of industry have significantly increased air pollution. This pollution affects human life and affects many life forms and makes the world uninhabitable. At this point, air pollution should be considered besides water pollution (1, 2).

Adsorption is an important process widely used in both water and air pollution removal. Thanks to this process, the polluted water has been cleaned and re-used for many years, even the existing swamps and the water communities that cannot be used are reintroduced as drinking water. Activated carbon has an important role in the adsorbents used for this purpose. Activated

carbon is the most widely used in adsorbents due to its micro and meso pore structure with high surface area (1, 2). Activated carbon is generally derived from coal and biomass and in recent years it has been started to be obtained from waste polymers. The variety and amount of biomass has become important in the production of activated carbon. The need for annual global activated carbon needs of 3 million tons and a 7% growth each year led to the increase in raw material diversity and even the use of all carbon containing waste for this purpose. As a result, both waste materials will be freed and these substances will be evaluated and re-used. In addition, the synthesis methods developed by these sources are gaining importance in increasing both surface areas and pore sizes of the adsorbents obtained from these sources. Agricultural wastes, especially found in our country, are very suitable for active carbon synthesis (3-11). The reason for this is the high amount of agricultural waste used as raw material and the carbon content of these wastes is suitable for the production of activated carbon (12-14).

Chemical and physical activation methods are generally used in the production of activated carbon (15, 16). In the physical activation, the carbonization process of the raw materials in different temperature ranges is found in the literature (17-19). The liquid and gas released during the process are used directly in the production of energy (20). The carbonized samples may be subjected to activation at different temperatures using steam and / or carbon dioxide. Changes in surface area can be seen depending on the activation method used (21-23).

In this study, biomass pistachio shell was used as the raw material. Activation of carbon dioxide was carried out after carbonization and activated carbon was produced as molecular sieve. In the carbonization process, pyrolysis gas yield, condensable pyrolysis oil yield and solid (char) yield were calculated. The activated carbon yield was calculated after activation. Surface area of activated carbon, FTIR, XRD, SEM characterization was evaluated.

EXPERIMENTAL AND THEORETICAL STUDIES

100 kg of pistachio shell was taken without taking any action (original moisture weight 4.97 %) and it was used in the experiments. Carbonization was carried out using a cylindrical furnace with a temperature adjustment of three zones. The steel reactor has an internal diameter of 8.2 cm and is suitable for gas inlet and condensable liquid outlet. A liquid fraction was collected which could be condensed by attaching two coolers to the reactor outlet. Activation was performed in a separate three-zone cylindrical furnace in quartz glass tube (inner diameter: 4 cm).

Surface area measurements of activated carbon samples were made by the Micromeritics TriStar 3000 surface analyzer. The surface area was determined from isotherm using the BET method (S_{BET}). Ash determination was made according to ASTM D2866-11 standard at 650°C. XRD measurements were made in Japanese Rigaku RadB-DMAX II (Cu K-alpha) system.

RESULTS AND DISCUSSION

Solid (char), liquid and gas yield results of carbonization samples is given in the Table 1.

Table 1: Solid (char), liquid and gas yield results of carbonized samples.

Temperature	N_2 Flowrate	Char Yield %	Liquid Yield %	Gas Yield %
300 °C	100 mL / min	40.89	37.85	21.26
400 °C	100 mL / min	29.63	43.94	26.43
500 °C	100 mL / min	25.69	43.11	31.20
600 °C	100 mL / min	24.05	48.04	27.91
700 °C	100 mL / min	23.10	39.85	37.05
800 °C	100 mL / min	23.30	36.90	39.80
900 °C	100 mL / min	23.67	40.67	35.66
1000 °C	100 mL / min	23.36	37.89	38.75
1000 °C	500 mL / min	22.77	36.83	40.40

As the temperature changes, the solid and liquid yield was varied. While this change is generally in the decrease in solid yield, decreases and increases in gas and liquid yield were observed. This situation can be explained by the deformation of the macromolecular structure with the effect of temperature. In addition, at high temperature (900 °C and above), the efficiency of the liquid decreases while the efficiency of the gas increases. Small groups are separated from the macromolecular structure at high temperature and passed to the gas phase. This reduces the liquid yield and increases the gas efficiency (24-26).

Table 2: BET analysis results of samples.

Carbonization		Physical Activation							
Temperature °C	N_2 Flowrate (mL/min)	Temperature °C (100 mL/min CO_2)	S_{BET} m^2/g	S_{micro} m^2/g	S_{meso} m^2/g	V_T cm^3/g	V_{micro} cm^3/g	V_{meso} cm^3/g	dp[a] nm
300	100	800	394.64	343.44	51.20	0.21	0.18	0.03	2.20
300	100	900	530.57	439.81	90.76	0.28	0.23	0.05	2.18
400	100	800	401.71	365.00	36.71	0.21	0.19	0.02	2.15
500	100	800	759.74	12.76	746.98	0.75	0.04	0.71	4.06
600	100	800	857.13	788.98	68.14	0.41	0.09	0.32	2.07
700	100	900	473.93	413.38	60.55	0.24	0.21	0.03	2.04
800	100	900	518.70	448.55	70.15	0.27	0.23	0.04	2.13
900	100	800	179.62	179.62	-	-	0.15	-	-
1000	500	800	16.66	16.66	-	-	0.04	-	-
1000	500	900	295.40	295.40	-	-	0.18	-	-

S: Surface area, V: volume dp: average pore diameter a: (4 V/A by BET)

When the results in Table 2 were examined, the total pore volume (V_T) was low at the low carbonization temperature while the micro pore surface area (S_{micro}) was maximum. The highest surface area was obtained for the sample synthesized at an activation temperature of 800 °C and a carbonization temperature of 600 °C. The micro pore surface area of the sample covers 92.04% of the total area. The average pore diameter is 2.04 nm and the pore size distribution is very narrow. As a result, carbonization and subsequent activation of carbon dioxide yielded molecular sieve activated carbon with nano-pore. DFT (Density Functional Theory) measurements of some activated carbons were obtained and as a result of these measurements, the presence of micropores in the structure was proven. The majority of the pore size are between 1-2 nanometers. The some sample of pore size distribution graph is given in Figure 1. Figure 2 shows the typical adsorption isotherm of N_2

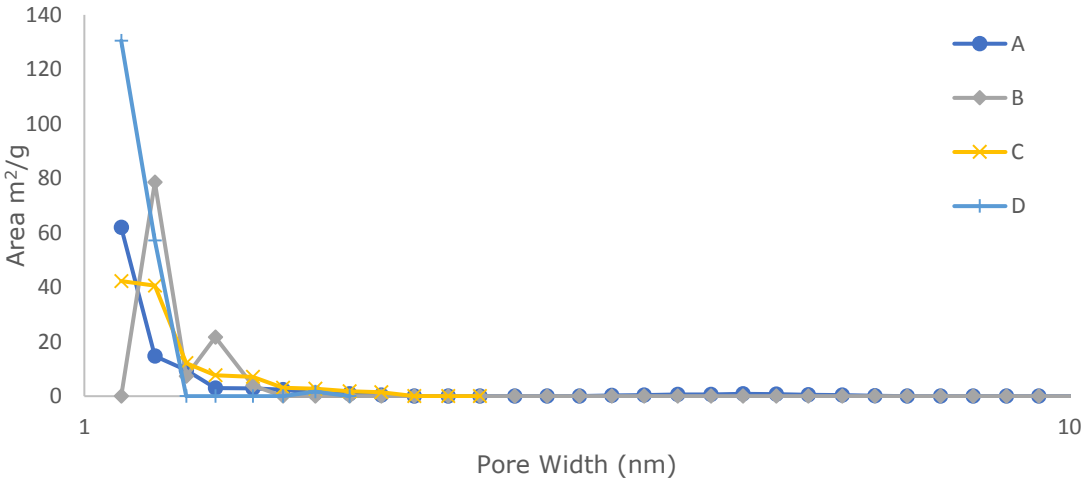

Figure 1: Pore size distribution of activated carbon sample **A.** at 300 °C 100 ml / min N_2 carbonization and at 800°C with 100 mL / min CO_2 activation **B.** at 600 °C 100 mL / min N_2 carbonization and at 800 °C with 100 mL / min CO_2 activation. **C**. at 800 °C 100 mL / min N_2 carbonization and at 900 °C with 100 mL / min CO_2 activation, **D.** at 900 °C 100 mL / min N_2 carbonization and at 800 °C with 100 mL / min CO_2 activation.

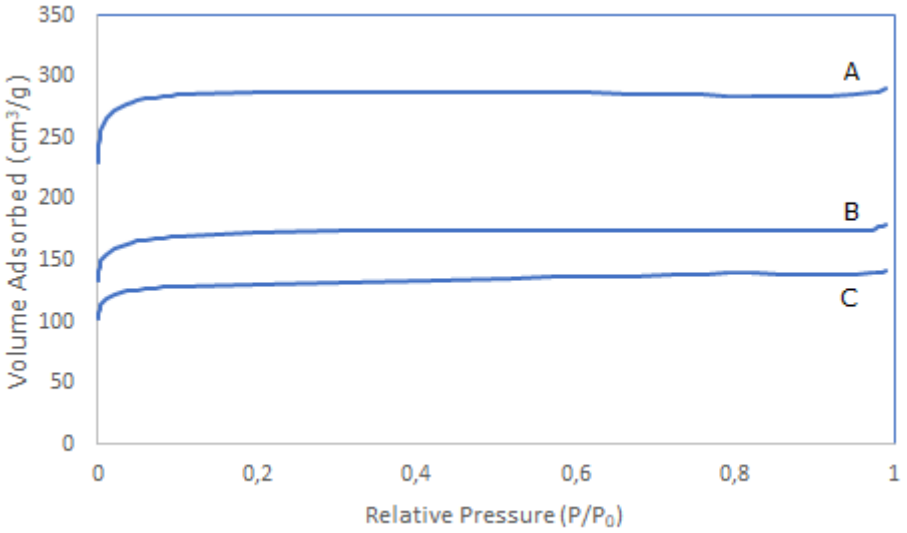

Figure 2: Adsorption isotherms of N_2 **A**. Activated carbon sample at 600 °C 100 mL / min N_2 carbonization and at 800°C with 100 mL / min CO_2 activation **B.** Activated carbon sample at 800 °C 100 mL / min N_2 carbonization and at 900 °C with 100 mL / min CO_2 activation. **C**. Activated carbon sample at 300 °C 100 mL / min N_2 carbonization and at 800 °C with 100 mL / min CO_2 activation.

When the adsorption isotherms were taken into consideration, it was determined that the samples obtained corresponded to the Type 1 isotherm (27-29). The general feature of the Type I isotherm is that it contains large amounts of micropores in the structure of the adsorbent. At low P / Po values, adsorption increased and then isotherm were on a flat plateau. As the P / Po value increases, the increase in adsorption is explained by the regularity of the pore size distribution (30-32).

Figure 3 shows the FTIR spectrum of raw material and activated carbon samples. FTIR spectra seen around 3600 cm^{-1} seen from the peak cellulosic structure belong to O-H groups. As a result of the structural arrangement resulting from the heat treatment, the hydroxyl groups were greatly reduced. The peaks at about 2900 cm^{-1} indicate the aliphatic C-H strength. These peaks are increased by the introduction of the raw material into the structural arrangement. The increase of aliphatic strength peaks with the increase in temperature is another proof of structural regulation. In addition, multiple peaks at this wavelength result from the vibration of the methylene groups. Similarly, peaks at this wavelength result from the vibration of peaks such as $-CH_3$, $-CH_2CH_3$ and $-CH_2$. The peaks at approximately 1000 cm^{-1} show that there is a C-C bond in the structure (33-35). When these results were taken into consideration, it was seen that the structure was similar to each other.

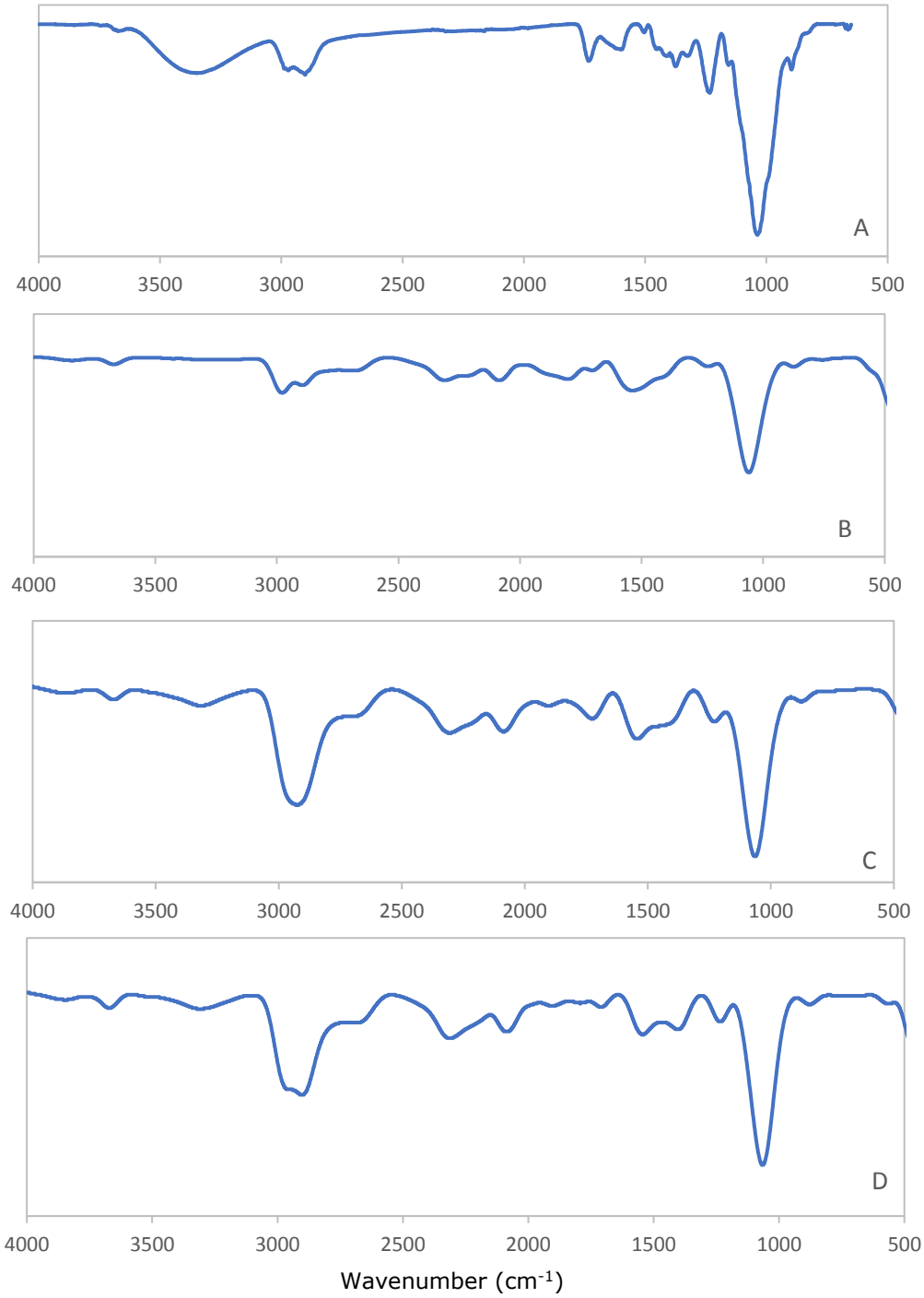

Figure 3: FTIR spectrum of raw material and activated carbon samples. **A.** Raw Pistachio Shell **B.** Activated carbon sample at 500 °C 100 mL / min N_2 carbonization and at 800°C with 100 mL / min CO_2 activation **C.** Activated carbon sample at 600 °C 100 mL / min N_2 carbonization and at 800 °C with 100 mL / min CO_2 activation **D.** Activated carbon sample at 1000 °C 500 mL / min N_2 carbonization and at 900 °C with 100 mL / min CO_2 activation.

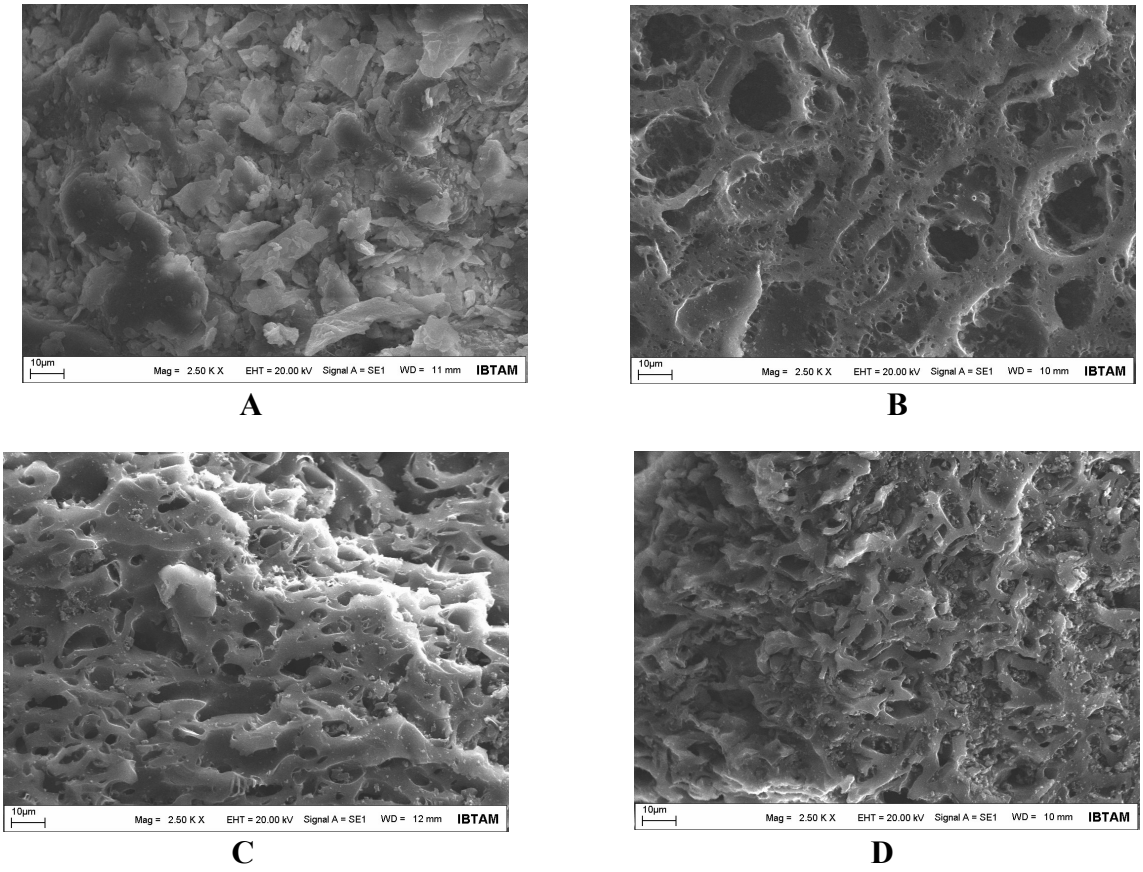

Figure 4: A. SEM image of raw pistachio shell **B.** Activated carbon sample at 600 °C 100 ml / min N_2 carbonization and at 800 °C with 100 mL / min CO_2 activation **C** Activated carbon sample at 500 °C 100 mL / min N_2 carbonization and at 800 °C with 100 mL / min CO_2 activation **D.** Activated carbon sample at 300 °C 100 mL / min N_2 carbonization and at 800 °C with 100 mL / min CO_2 activation.

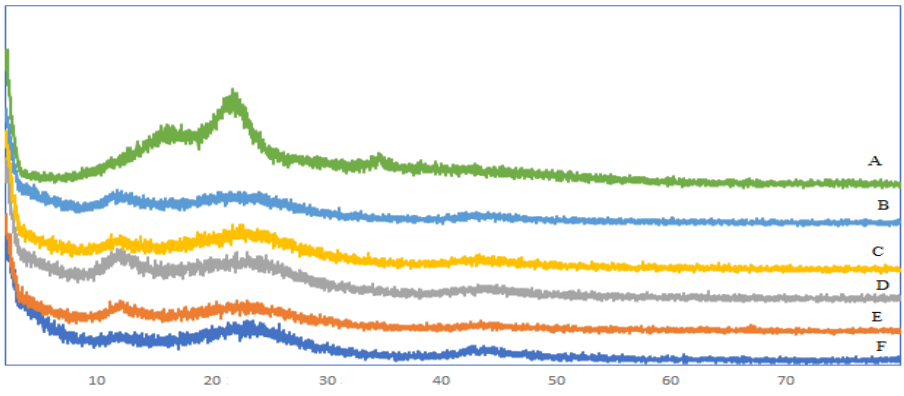

Figure 5: XRD chart of samples **A.** XRD chart of raw pistachio shell **B.** Activated carbon sample at 400 °C 100 mL / min N_2 carbonization and at 800 °C with 100 mL / min CO_2 activation **C.** Activated carbon sample at 500 °C 100 mL / min N_2 carbonization and at 800 °C with 100 mL / min CO_2 activation i **D.** Activated carbon sample at 600 °C 100 mL / min N_2 carbonization and at 800 °C with 100 mL / min CO_2 activation **E.** Activated carbon sample at 900 °C 100 mL / min N_2 carbonization and at 800 °C with 100 mL / min CO_2 activation **F.** Activated carbon sample at 1000 °C 500 mL / min N_2 carbonization and at 900 °C with 100 mL / min CO_2 activation.

In the SEM images shown in Figure 4, no visible pores are present in the pistachio shell used as raw material. But carbonization and physical activation result in the formation of pores. With the increase in temperature, it is seen that pores appear as a result of the separation of small organic groups within the macromolecular structure. In the original macromolecular structure of pistachio, it is concluded that the pores have the same size as the molecular units are composed of structures of similar size. The homogeneity of the pores shows that the

activated carbon is in the form of a molecular sieve.

Figure 5 shows the XRD graphs of raw materials and activated carbon samples. As can be understood from the XRD plot of raw pistachio, the structure is largely amorphous. 3 different amorphous structures in the structure can be expressed as macromolecular groups. Crystalline units are separated from the structure with the effect of temperature and the structure turns into completely amorphous structure. As in the original raw sample, three different macromolecular main units remain in the structure (36, 37).Table 3 shows the ash values of samples

Table 3: Ash values of samples.

Carbonization		Physical Activation	
Temperature (°C)	N_2 Flow rate (mL/min)	Temperature (°C) Gas Flow rate (100 mL/min CO_2)	Ash %
	Raw pistachio shell		0.380
300	100	800	0.020
300	100	900	0.019
400	100	800	0.017
500	100	800	0.019
600	100	800	0.019
700	100	900	0.018
800	100	900	0.024
900	100	800	0.028
1000	500	800	0.020
1000	500	900	0.025

When the ash values of the samples are examined, the ash value of the raw materials is high but the ash values of the synthesized materials are lower than the raw materials. It can be explained by the fact that the inorganic components forming the ash in the structural arrangement are inorganic elements degraded at high temperature and also they are in organic chelate structure. Low temperature ash can be explained by the chelate structure. At high temperature, the mass increased due to the loss of organic structure. The elemental analysis results of samples is given in Table 4.

Table 4: Elemental analysis results of samples.

Samples		**%C**	**%H**	**%N**	**%S**	**%O***
Raw Pistachio Shell		47.37	5.896	-	-	46.734
300 °C	100 mL/min N_2 800°C CO_2	58.39	1.102	-	-	40.508
300 °C	100 mL/min N_2 900°C CO_2	88.98	0.717	-	-	10.303
400 °C	100 mL/min N_2 800°C CO_2	65.61	1.157	0.144	-	33.089
500 °C	100 mL/min N_2 800°C CO_2	89.84	1.109	-	-	9.051
600 °C	100 mL/min N_2 800°C CO_2	86.57	1.131	-	-	12.299
700 °C	100 mL/min N_2 800°C CO_2	87.11	1.049	0.124	-	11.717
900 °C	100 mL/min N_2 800°C CO_2	64.49	0.803	0.308	-	34.399
1000 °C	500 mL/min N_2 800°C CO_2	58.07	0.789	0.599	-	40.542
1000 °C	500 mL/min N_2 900°C CO_2	68.85	0.658	0.348	-	30.144

* *Calculated by difference*

Considering the results of the elemental analysis, it was observed that the percentage of carbon in the synthesized materials increased as compared to the raw material. In addition, there is a decrease in the amounts of hydrogen and oxygen. The decrease in their amounts indicates structural regulation. Methylene blue adsorption capacity of samples is in Table 5.

.

Table 5: Methylene blue adsorption capacity of samples.

Carbonization		Physical Activation		
Temperature (°C)	N_2 Flow rate (mL/min)	Temperature (°C) Gas Flow rate (100 mL/min CO_2)	S_{BET} m^2/g	Adsorption Capacity q_e (mg/g)
300	100	800	394.64	25.31
300	100	900	530.57	93.45
400	100	800	401.71	19.48
600	100	800	857.13	5.95
700	100	900	473.93	68.54
800	100	900	518.70	91.16
900	100	800	179.62	32.79
1000	500	800	16.66	1.77
1000	500	900	295.40	19.59

Methylene blue adsorption on samples was studied. 0.1 gram of active carbon samples were taken into 100 mL 100 ppm methylene blue solution and samples were measured after 24 hours. In the results, the adsorption capacity of methylene blue was calculated and given as a table. As seen in the BET measurements and DFT measurements, the working samples have the majority of micro pores and their adsorption capacity is low. Methylene blue is a compound with a molecule size of approximately 1.43 nm (38, 39) and methylene blue molecules do not enter the pore (40). Therefore, their adsorption capacity is low.

ACKNOWLEDGEMENT

This study was supported by the unit of Scientific Researches of Inonu University in Malatya, Turkey; Project no: FDI-2017-680

REFERENCES

1. Dias JM, Alvim-Ferraz MC, Almeida MF, Rivera-Utrilla J, Sánchez-Polo M. Waste materials for activated carbon preparation and its use in aqueous-phase treatment: a review. Journal of environmental management. 2007;85(4):833–846.

2. Rafatullah M, Sulaiman O, Hashim R, Ahmad A. Adsorption of methylene blue on low-cost adsorbents: a review. Journal of hazardous materials. 2010;177(1–3):70–80.

3. Yagmur E, Ozmak M, Aktas Z. A novel method for production of activated carbon from waste tea by chemical activation with microwave energy. Fuel. 2008 Nov;87(15–16):3278–85.

4. Özdemir M, Bolgaz T, Saka C, Şahin Ö. Preparation and characterization of activated carbon from cotton stalks in a two-stage process. Journal of Analytical and Applied Pyrolysis. 2011;92(1):171–175.

5. Şahin Ö, Saka C. Preparation and characterization of activated carbon from acorn shell by physical activation with H2O–CO2 in two-step pretreatment. Bioresource technology. 2013;136:163–168.

6. Dolas H, Sahin O, Saka C, Demir H. A new method on producing high surface area activated carbon: The effect of salt on the surface area and the pore size distribution of activated carbon prepared from pistachio shell. Chemical engineering journal. 2011;166(1):191–197.

7. Gonzalez JF, Roman S, González-García CM, Nabais JV, Ortiz AL. Porosity development in activated carbons prepared from walnut shells by carbon dioxide or steam activation. Industrial & engineering chemistry research. 2009;48(16):7474–7481.

8. Kütahyalı C, Eral M. Sorption studies of uranium and thorium on activated carbon prepared from olive stones: kinetic and thermodynamic aspects. Journal of Nuclear Materials. 2010;396(2–3):251–256.

9. Şayan E. Ultrasound-assisted preparation of activated carbon from alkaline impregnated hazelnut shell: An optimization study on removal of Cu2+ from aqueous solution. Chemical Engineering Journal. 2006;115(3):213–218.

10. Georgin J, Dotto GL, Mazutti MA, Foletto EL. Preparation of activated carbon from peanut shell by conventional pyrolysis and microwave irradiation-pyrolysis to remove organic dyes from aqueous solutions. Journal of Environmental Chemical Engineering. 2016;4(1):266–275.

11. Depci T, Onal Y, Prisbrey KA. Apricot stone activated carbons adsorption of cyanide as revealed from computational chemistry analysis and experimental study. Journal of the Taiwan Institute of Chemical Engineers. 2014 Sep;45(5):2511–7.

12. Kadirvelu K, Kavipriya M, Karthika C, Radhika M, Vennilamani N, Pattabhi S. Utilization of various agricultural wastes for activated carbon preparation and application for the removal of dyes and metal ions from aqueous solutions. Bioresource Technology. 2003 Mar;87(1):129–32.

13. Ioannidou O, Zabaniotou A. Agricultural residues as precursors for activated carbon production—A review. Renewable and Sustainable Energy Reviews. 2007 Dec;11(9):1966–2005.

14. Yahya MA, Al-Qodah Z, Ngah CWZ. Agricultural bio-waste materials as potential sustainable precursors used for activated carbon production: A review.

Renewable and Sustainable Energy Reviews. 2015 Jun;46:218–35.

15. Kilic M, Apaydin-Varol E, Pütün AE. Adsorptive removal of phenol from aqueous solutions on activated carbon prepared from tobacco residues: Equilibrium, kinetics and thermodynamics. Journal of Hazardous Materials. 2011 May;189(1–2):397–403.

16. Rodríguez-Reinoso F, Molina-Sabio M. Activated carbons from lignocellulosic materials by chemical and/or physical activation: an overview. Carbon. 1992;30(7):1111–8.

17. Bouchelta C, Medjram MS, Bertrand O, Bellat J-P. Preparation and characterization of activated carbon from date stones by physical activation with steam. Journal of Analytical and Applied Pyrolysis. 2008 May;82(1):70–7.

18. Thommes M. Physical Adsorption Characterization of Nanoporous Materials. Chemie Ingenieur Technik. 2010 Jun 14;82(7):1059–73.

19. Yun CH, Park YH, Park CR. Effects of pre-carbonization on porosity development of activated carbons from rice straw. Carbon. 2001 Apr;39(4):559–67.

20. Lee H, Kim Y-M, Kim S, Ryu C, Park S, Park Y-K. Review of the use of activated biochar for energyand environmental applications. Carbon Lett. 2018;26:1–10.

21. Marsh H, Rodríguez-Reinoso F. Activated carbon. 1st ed. Amsterdam ; Boston: Elsevier; 2006. 536 p.

22. Ahmadpour A, Do DD. The preparation of activated carbon from macadamia nutshell by chemical activation. Carbon. 1997;35(12):1723–32.

23. Pallarés J, González-Cencerrado A, Arauzo I. Production and characterization of activated carbon from barley straw by physical activation with carbon dioxide and steam. Biomass and Bioenergy. 2018 Aug;115:64–73.

24. Giudicianni P, Cardone G, Ragucci R. Cellulose, hemicellulose and lignin slow steam pyrolysis: Thermal decomposition of biomass components mixtures. Journal of Analytical and Applied Pyrolysis. 2013 Mar;100:213–22.

25. Burhenne L, Messmer J, Aicher T, Laborie M-P. The effect of the biomass components lignin, cellulose and hemicellulose on TGA and fixed bed pyrolysis. Journal of Analytical and Applied Pyrolysis. 2013 May;101:177–84.

26. Cabrales L, Abidi N. On the thermal degradation of cellulose in cotton fibers. Journal of Thermal Analysis and Calorimetry. 2010 Nov;102(2):485–91.

27. Rouquerol F, Rouquerol J, Sing KSW, Llewellyn PL, Maurin G. Adsorption by powders and porous solids: principles, methodology and applications. Second edition. Amsterdam: Elsevier/AP; 2014. 626 p.

28. Labani MM, Rezaee R, Saeedi A, Hinai AA. Evaluation of pore size spectrum of gas shale reservoirs using low pressure nitrogen adsorption, gas expansion and mercury porosimetry: A case study from the Perth and Canning Basins, Western Australia. Journal of Petroleum Science and Engineering. 2013 Dec;112:7–16.

29. Collet F, Bart M, Serres L, Miriel J. Porous structure and water vapour sorption of hemp-based materials. Construction and Building Materials. 2008 Jun;22(6):1271–80.

30. Saka C. BET, TG–DTG, FT-IR, SEM, iodine number analysis and preparation of activated carbon from acorn shell by chemical activation with ZnCl2. Journal of Analytical and Applied Pyrolysis. 2012 May;95:21–4.

31. Bansal RC, Goyal M. Activated carbon adsorption [Internet]. Boca Raton: Taylor & Francis; 2005 [cited 2019 Mar 23]. Available from: http://www.crcnetbase.com/isbn/9780824753443

32. Ahmedna M, Marshall W., Rao R. Production of granular activated carbons from select agricultural by-products and evaluation of their physical, chemical and adsorption properties1Louisiana Agricultural Experiment Station manuscript 99-21-0066.1. Bioresource Technology. 2000 Jan;71(2):113–23.

33. Zhang Z, Xu M, Wang H, Li Z. Enhancement of CO2 adsorption on high surface area activated carbon modified by N2, H2 and ammonia. Chemical Engineering Journal. 2010 Jun;160(2):571–7.

34. Lua AC, Guo J. Microporous Oil-Palm-Shell Activated Carbon Prepared by Physical Activation for Gas-Phase Adsorption. Langmuir. 2001 Oct;17(22):7112–7.

35. Nabais JMV, Nunes P, Carrott PJM, Ribeiro Carrott MML, García AM, Díaz-Díez MA. Production of activated carbons from coffee endocarp by CO2 and steam activation. Fuel Processing Technology. 2008 Mar;89(3):262–8.

36. Okada K, Yamamoto N, Kameshima Y, Yasumori A. Porous properties of activated carbons from waste newspaper prepared by chemical and physical activation. Journal of Colloid and Interface Science. 2003 Jun;262(1):179–93.

37. Lua AC, Yang T. Effects of vacuum pyrolysis conditions on the characteristics of activated carbons derived from pistachio-nut shells. Journal of Colloid and Interface Science. 2004 Aug;276(2):364–72.

38. Ferrero F. Adsorption of Methylene Blue on magnesium silicate: Kinetics, equilibria and comparison with other adsorbents. Journal of Environmental Sciences. 2010 Jan;22(3):467–73.

39. Raposo F, De La Rubia MA, Borja R. Methylene blue number as useful indicator to evaluate the adsorptive capacity of granular activated carbon in batch mode: Influence of adsorbate/adsorbent mass ratio and particle size. Journal of Hazardous Materials. 2009 Jun 15;165(1–3):291–9.

40. Ma J, Yu F, Zhou L, Jin L, Yang M, Luan J, et al. Enhanced Adsorptive Removal of Methyl Orange and Methylene Blue from Aqueous Solution by Alkali-Activated Multiwalled Carbon Nanotubes. ACS Applied Materials & Interfaces. 2012 Nov 28;4(11):5749–60.

JOTCS B
Journal of the Turkish Chemical Society
Section: B
Chemical Engineering
TURKISH CHEMICAL SOCIETY

Modification of Safflower Oil with Triallyl Ether Acrylate Dienophile

Gediz Uğuz[a*], Satılmış Basan[b]

[a]Department of Chemical Engineering, Ondokuz Mayis University, Samsun, TURKEY
[b*]Department of Chemical Engineering, Hittite University, Çorum, TURKEY

Abstract: Alkyd resins and reactive diluents, which are among the main components of dye and coating industries, have properties such as binding and ease of application. In order to improve the film properties of alkyd resins, a wide variety of modification studies are carried out. In this study, safflower oil was modified with triallyl ether acrylate dienophile (TAEA) with Diels - Alder reactions and the product was called as triallyl ether acrylate safflower oil (TAEASO) reactive diluent. TAEASO has been characterized by Nuclear Magnetic Resonance (NMR) and Fourier Transform Infrared Spectroscopy (FT-IR) techniques. Then, the different dye formulations were prepared with certain proportions of TAEASO, wetting and drying agents and a soy oil (SO) based alkyd resin. Dye formulations were called as SO, TAEASO10-SO, TAEASO20-SO, TAEASO30-SO, TAEASO40-SO. The viscosity reductions of the dye formulations were determined and then the dye formulations were applied to surface of aluminum plates as a film. The film properties such as drying time, film thickness, pencil hardness, brightness were evaluated after the curing process. The results show that the viscosity reduction is proportional to the ratio of the TAEASO. As a result of the study, the drying time for the reactive diluent with alkyds were 1.5 times faster than alkyd alone.

Keywords: Alkyd, Diels-Alder, safflower, triallyl ether acrylate.

Submitted: March 26, 2019. **Accepted:** May 16, 2019.

Cite this: Uğuz G, Basan S. Modification of Safflower Oil with Triallyl ether acrylate Dienophile. JOTCSB. 2019;2(1):45–50.

***Corresponding author. E-mail:** gedizuguz55@gmail.com. Tel : + 90 545 5585519.

INTRODUCTION

In recent years, many studies have been carried out to develop an "environmentalist" dye and coating systems (1, 2). In these studies, seed oils are considered as an alternative since they are biodegradable, easily accessible, and renewable. Seed oils are divided into three different categories: drying, half-drying and non-drying according to the number of unsaturated bonds in the fatty acid chain. In the production of binders that are important for the dye and coating industry, seed oils with a high number of unsaturated bonds such as safflower oil, soybean oil, flax oil and tung oil are widely used. The binders produced with these oils form the polymer film easier when applied to the surfaces, thus increasing the drying rate and reducing the drying time. The formation of a polymer film containing a seed oil-based binder is called an auto-oxidative curing.

The auto-oxidation process first begins with the attack of the molecular oxygen to the unsaturated bonds in the fatty acid chain and then is followed by homolytic cleavage of the peroxide to form free radicals. The hydrogen is then separated by isomerization from the methylene group between the C-C bonds (2, 3).

The safflower plant is connected to the family named Compositae (Asteraceae) in Latin and can be planted annually, winter and summer. The oil content of this plant is about 25-27%. This rate has reached up to 46-47% with scientific researches (4). The safflower, which is light in color, has an important place among the oil crops due to its high content of linoleic

acid (5). The proportion of linoleic acid and oleic acid in safflower oil is 81% and 10%, respectively. Safflower oil is in the class of drying oils due to its high rate of linoleic acid. Drying oils contain many double bonds in their structures. Linoleic acids are called diene according to the number of double bonds they contain in their structures.

Diels-Alder reactions are a cyclo-addition reactions commonly known in organic chemistry, based on the formation of a ring structure by conjugated diene and dienophile (6-9).

The aims of this study was to develop new materials to replace the need for organic solvents in alkyd-based coatings with more environmentalist reactive diluents and improve the film properties of alkyd resins (10-12). In this study, safflower oil was modified with triallyl ether acrylate dienophile (TAEA) with Diels - Alder reactions and the product was called as triallyl ether acrylate safflower oil (TAEASO) reactive diluent. TAEASO has been characterized by NMR and FT-IR techniques. It was investigated that TAEASO cannot be used as a reactive diluent in alkyd systems. The film properties (viscosity reduction, drying time, gloss and pencil hardness) of alkyd films prepared with TAEASO were investigated.

EXPERIMENTAL

Material and methods

Safflower oil has been obtained from Kayseri in Turkey. Phenothiazine, pentaerythritol triallyl ether (PETAE), acrylic acid (AA), dichloromethane and p-toluene sulfonic acid (p-TSA) have been purchased from Sigma Aldrich.

General procedure

Triallyl ether acrylate (TAEA) modified safflower oil has been prepared by two-step reactions. In the first step TAEA was prepared by esterification of PETAE with AA. PETAE (100 g), AA (56.16 g), phenothiazine (1 g), p-toluenesulfonic acid (0.67 g), and dichloromethane (200 mL) were mixed in a three-neck round flask and heated to reflux. The reaction was kept at reflux for 3 h and cooled to room temperature. Dichloromethane was removed in vacuum. Anhydrous diethyl ether (200 mL) was added, and then slowly 5% sodium carbonate solution (200 mL). The organic layer was washed with deionized water (3x200 mL) and dried with anhydrous $MgSO_4$ (50 g). The solvent was removed in vacuum to give triallyl ether acrylate (TAEA) as shown in Figure 1. In a second step, safflower oil (80 g) and obtained TAEA (28 g, 0.09 mol) were added into 250 mL three-necked round flask equipped with stirrer, condenser, and thermocouple. The flask was mixed for 15 min under nitrogen purge, then the temperature was raised to 120 ^oC and kept for 2 h. The obtained reactive diluent was cooled to room temperature and characterized by ^1H-NMR, ^{13}C-NMR and FT-IR.

TAEA modified safflower oil (TAEASO) was formulated with the alkyd resin at four different ratios (10, 20, 30 and 40 wt.-% based on total formulation), 2 % metal drier package (10% cobalt, 80% zirconium, 10% calcium) and 1 % wetting agent. The samples have been applied on flat aluminum plates with a paint applicator in the form of approximately 150 µm thick film and cured at 160 ^oC and kept for 3 h.

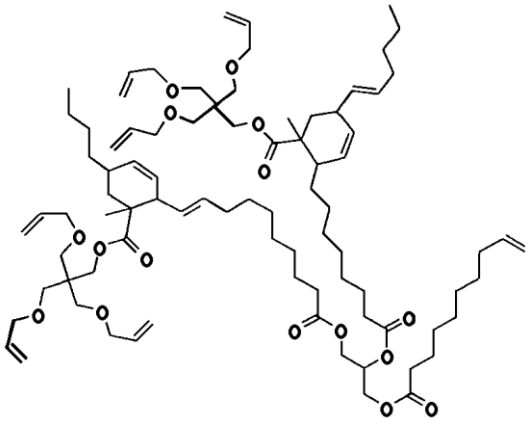

Figure 1: Structures of reactive diluent synthesized via the Diels–Alder reaction: triallyl ether acrylate (TAEA) modified safflower oil.

Characterization

In Diels-Alder reactions, linoleic acid ratio in safflower oil, which acts as diene, has been determined using SGE, BPX70 capillary column (60 m x 0.25 mm x 0.25 µm) with Perkin Elmer Clarus 680 model gas chromatography (GC) device. The method used in GC is TS EN ISO 12966-2. In addition,

the characterization of synthesized reactive diluent is in the range of 4000-650 cm^{-1} wavenumber, the resolution is 4 cm^{-1}, and in 4 scans the Bruker AVANCE III 400 MHz device with Perkin Elmer Fourier Transform Infrared Spectroscopy (FT-IR) and ^{1}H, ^{13}C, ^{19}F and ^{31}P probes and Nuclear Magnetic Resonance (NMR) device have been used.

Data for ^{1}H and^{13}C have been recorded between -2.00 and 10.00 parts per million (ppm) and -10.00 to 150.00 ppm for 500 MHz frequency. The viscosity measurements of the resin samples were made using L4 coded spindle at a speed of 20 rpm with the use of the Fungilab S.A. V.1.2 Alpha Series viscometer at 25 °C. The determination of drying time of films formed as a result of application of resin samples has been made at 20 ± 1 °C in according to DIN standard (DIN 53 150).

RESULTS AND DISCUSSION

The use of reactive diluent obtained by Diels-Alder reaction with TAEA dienophile of safflower oil as an alternative diluent in alkyd resins has been investigated in this study. The double bond ratio is important in terms of efficiency in improving the drying properties of alkyd resin. Therefore, the double bond ratio determined in GC is shown in **Table 1.**

Table 1: Fatty acid compositions of safflower oil.

Sample	Fatty acid	Fatty acid (%)
Safflower oil	Oleic acid (C18:1)	17.99
	Linoleic acid (C18:2)	72.61
	Palmitic acid (C16:0)	6.55
	Stearic acid (C18:0)	2.43
	Arachidic acid (C20:0)	0.32
	Myristic acid (C14:0)	0.09

Fatty acid compositions of drying oils are different from each other. As with the Diels-Alder reaction carried out by Brunner and Tucker between tung oil and styrene, the double bonds in dienes react with dienophiles. Depending on the presence of double bonds, three different (alkyl siloxane, triallyl ether acrylate, and fluorinated alkyl) groups with Tung oil acrylate monomer have been functionalized with Diels-Alder reactions to form the new three reactive diluents (13).

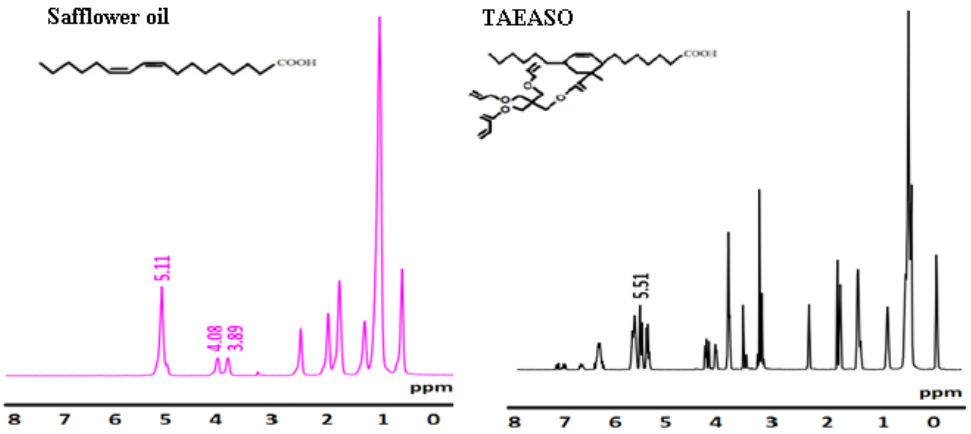

Figure 2: ^{1}H-NMR spectra of safflower oil and TAEASO.

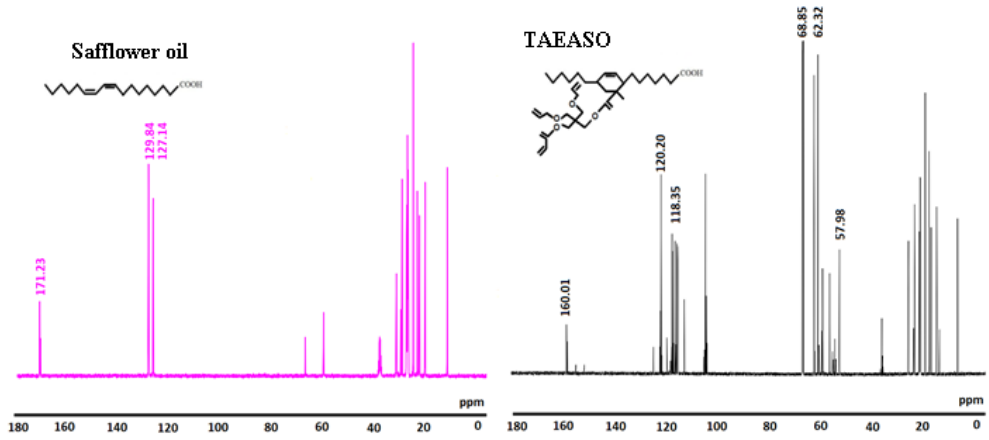

Figure 3: ^{13}C-NMR spectra of safflower oil and TAEASO.

Figure 2 and **3** show ^{1}H-NMR and ^{13}C-NMR spectra of safflower oil alkyd for comparison with the Diels–Alder adducts.

Figure 2 shows the ^{1}H-NMR spectra of safflower oil and TAEASO. The Diels- Alder reaction between dienophiles and safflower oil take results in the reduction of the resonances of conjugated double bonds at nearly 5.11 ppm. New resonances appear at nearly 5.51 ppm respectively due to the cyclohexene ring created during the Diel-Alder reaction. Most of the peaks are assigned to the structure of Triallyletheracrylate modified safflower oil in **Figure 2.**

Further analysis was performed via ^{13}C-NMR. **Figure 3** shows the ^{13}C NMR spectra of safflower oil and TAEASO. The assigned peak of ^{13}C-NMR of safflower oil is shown in **Figure 3**. The resonance at nearly corresponds to the unsaturated carbon, the resonance at nearly 160.01 ppm is due to the carbonyl groups in safflower oil. Comparing to the assigned ^{13}C-NMR spectra of reactive diluents with safflower oil shown in Figure 4, a new carbonyl group appears at nearly 120.20 ppm corresponding to the attachment of TAEASO to the safflower oil back bone (8).

FT-IR spectra of safflower oil and TAEASO are shown in **Figure 4**. and **Table 2.** FT-IR was used to determine crosslinking bonds situation with triallyl ether acrylate addition (14).

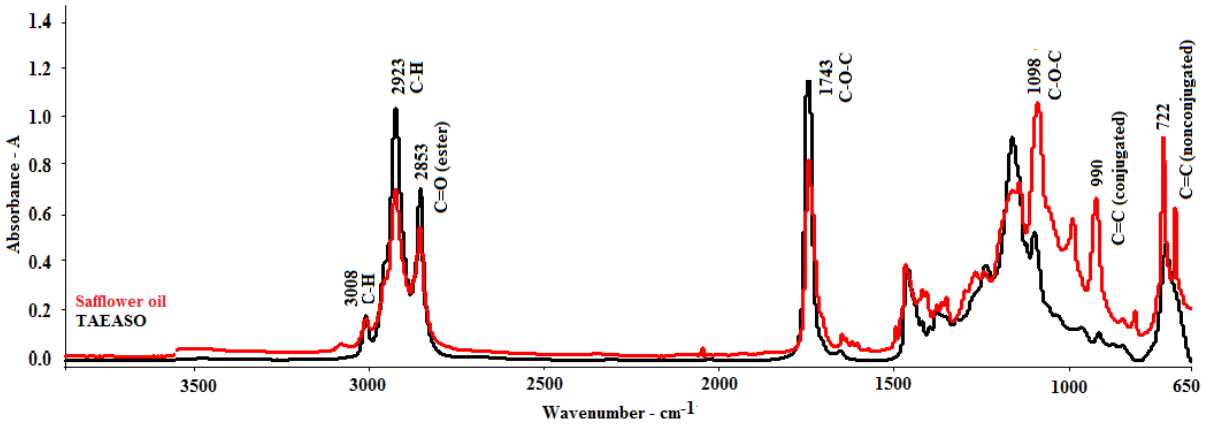

Figure 4: FT-IR spectra of safflower oil and TAEASO.

Table 2: FT-IR spectra of safflower oil and TAEASO.

Wavenumber (cm^{-1})	Functional group
3008	C-H
2923	C-H
2853	CH_2
1743	C=O (Ester)
1180	C-O-C
1098	C-O-C
990	C=C (conjugated double bonds)
722	C=C (non-conjugated double bonds)

In **Figure 4**, the band at 990 cm^{-1} was attributed to conjugated double bonds (8). 722 cm^{-1} are attributed to cis-C=CH bending. In the course of the Diels-Alder, conjugated double bonds were greatly reduced which indicated the cycloaddition to the safflower oil (13). The cycloaddition indicates the consumption of double bonds in the fatty acids as a result of autoxidative crosslinking (15).

Properties of dye formulations

In recent years, manufacturers have been trying to reduce the cost of alkyd resins. They make new attempts to improve the film properties of alkyd resins and to enhance their usage in coating applications (16-20). The solution and film properties such as viscosity, drying time, gloss, thickness and pencil hardness of dye formulations containing TAEA in different ratios were investigated and the results obtained are given in **Table 3.**

Viscosity reduction is expected by addition of reactive diluents to alkyd resins. Alkyd resins containing certain proportions of reactive diluents have been compared with neat alkyd. The viscosity of the samples has been investigated as a function of the dienophile amount. The results are shown in Table 3. The viscosity of neat alkyd has been measured approximately 1603 cP. Addition of reactive diluent to alkyd has reduced viscosity as expected. The maximum viscosity reduction rates in alkyd containing, TAEASO10-SO, TAEASO20-SO, TAEASO30-SO and TAEASO40-SO, are 37%, 55% 71% and 75%, respectively. The reason for this difference is the involvement of conjugation and the cycloaddition in Diels-Alder reactions of safflower oil with dienophile.

According to these results, it is considered that reactive diluents obtained can replace organic solvents used as diluents in the alkyd.

Table 3: Viscosity, viscosity reduction, drying time and film properties of alkyd and alkyd/diluent mixtures.

Sample	Viscosity Reduction %	Drying Time, hour	20º Gloss	60º Gloss	Pencil Hardness
SO	-	21	101,3	90,3	2B
TAEASO10-SO	37	13	110,3	101,1	B
TAEASO20-SO	55	14	110,2	100,3	B
TAEASO30-SO	71	15	102,4	91,8	B
TAEASO40-SO	75	15	101,3	90,7	B

As a result of Diels-Alder reactions of safflower oil with reactive diluents, the cross-linking mechanism has been changed. Therefore, it is important to investigate the drying time. Drying time experiments have been carried out in room conditions (25 ºC).

The results of drying time are shown in **Table 3** drying is directly related to the reduction of safflower oil added into the alkyd and reduction of viscosity. TAEASO containing alkyd resins have a drying time of more than 24 hours. The drying time of alkyd containing TAEASO is about 1.5 times less than the drying time of the alkyd without the reactive diluent. This is the result of the presence of more reactive groups in TAEASO.

CONCLUSIONS

Diels-Alder reactions have been used for the modification of safflower oil with TAEA dienophile in certain proportions. Dienophile including acrylate molecule, triallyl ether acrylate (TAEA), have been used to determine the ability to cycloaddition of the safflower oil with Diels-alder reactions at chosen temperature and atmospheric pressure. The experimental conditions have been determined by taking into account the physicochemical properties of the acrylate molecule. As a result of the study, it has been determined that the viscosity reduction in alkyd resins with reactive diluent may reach up to 75%. In addition, it has been observed

that drying time decreases by addition of reactive diluents into alkyd resins. Additional TAEA dienophile properties such as the gloss appear to not be significantly affected by the diluent content. The neat alkyd films have same thickness as those films that contain the reactive diluents in certain proportions. The pencil hardness of the films improved as predicted for the reactive diluents.

ACKNOWLEDGEMENT

This study was supported by the unit of Scientific Researches of Hittite University in Çorum, Turkey; Project no: FBE19004.17.002.

REFERENCES

1. Muizebelt WJ, Hubert JC, Nielen MWF, Klaasen RP, Zabel KH. Crosslink mechanisms of high-solids alkyd resins in the presence of reactive diluents. Progress in Organic Coatings. 2000 Dec;40(1–4):121–30.

2. Teng G, Soucek M, Vick B, Simonsick W, Sen A. Spectroscopic investigation of the blowing process of soyabean oil. Surface Coatings International Part B: Coatings Transactions. 2003 Sep;86(3):221–9.

3. Martyak NM, Alford D, Picker R, Dowling C. Controlled oxidative curing of tung oil. JCT coatingstech. 2005;2(16):36–41.

4. Mallegol J, Gonon L, Commereuc S, Verney V. Thermal (dsc) and chemical (iodometric titration) methods for peroxides measurements in order to monitor drying extent of alkyd resins. Progress in Organic Coatings. 2001;41(1–3):171–6.

5. Metcalfe DS, Elkins DM, Hughes HDM. Crop production: principles and practices. 4th ed. New York: Macmillan; 1980. 774 p.

6. Muizebelt WJ, Donkerbroek JJ, Nielen MWF, Hussem JB, Biemond MEF, Klaasen RP, et al. Oxidative crosslinking of alkyd resins studied with mass spectrometry and NMR using model compounds. J Coatings Tech. 1998 Jan;70(1):83–93.

7. Muizebelt W, Nielen MWF. Oxidative Crosslinking of Unsaturated Fatty Acids Studied with Mass Spectrometry. Journal of Mass Spectrometry. 1996;31(5):545–54.

8. Wutticharoenwong K, Dziczkowski J, Soucek MD. Tung based reactive diluents for alkyd systems: Film properties. Progress in Organic Coatings. 2012 Apr;73(4):283–90.

9. Ni H, Skaja A, Soucek M, Simonsick W, Zhong W. Alkoxysilane-modified polyurea coatings. Polymeric Materials Science and Engineering[Polym Mater Sci Eng]. 1999;81:405–406.

10. Wold CR, Soucek MD. Mixed metal oxide inorganic/organic coatings. J Coatings Tech. 1998 Jul;70(7):43–51.

11. Tuman S, Soucek M. Novel inorganic/organic coatings based on linseed oil and sunflower oil with sol-gel precursors. JCT, Journal of coatings technology. 1996;68(854).

12. Ballard RL, Tuman SJ, Fouquette DJ, Stegmiller W, Soucek MD. Effects of an Acid Catalyst on the Inorganic Domain of Inorganic−Organic Hybrid Materials. Chem Mater. 1999 Mar;11(3):726–35.

13. Wutticharoenwong K, Soucek MD. Synthesis of Tung-Oil-Based Reactive Diluents. Macromol Mater Eng. 2010 Dec 10;295(12):1097–106.

14. Salata R, Pellegrene B, Soucek M. Migration of fluorinated alkyd and fluorinated tung oil additives for partially self-stratifying coatings. Progress in Organic Coatings. 2019 Aug;133:406–17.

15. Salata RR, Pellegrene B, Soucek MD. Synthesis and properties of a high solids triethoxysilane-modified alkyd coatings. Progress in Organic Coatings. 2019 Aug;133:340–9.

16. Park HS, Jeon YJ, Kim SK, Kang DW. Synthesis and Physical Properties of Two-Component Polyurethane Coatings Containing Alkyd and Polyester Polyols. Korea Polym J. 1997;5(4):256–61.

17. Sailer RA, Soucek MD. Oxidizing alkyd ceramers. Progress in Organic Coatings. 1998 Jan;33(1):36–43.

18. Sailer RA, Wegner JR, Hurtt GJ, Janson JE, Soucek MD. Linseed and sunflower oil alkyd ceramers. Progress in Organic Coatings. 1998 Feb;33(2):117–25.

19. Thanamongkollit N, Soucek MD. Synthesis and properties of acrylate functionalized alkyds via a Diels–Alder reaction. Progress in Organic Coatings. 2012 Apr;73(4):382–91.

20. Wang C, Jones F. Stability and film properties of tung oil modified soybean alkyd emulsion. J Appl Polym Sci. 2000;78(9):1698–706.